International Journal of Nanomedicine

Dovepress
Taylor & Francis Group

Open Access Full Text Article

ORIGINAL RESEARCH

Tri-Functional MgTA@MnO_2 Nanozymes Orchestrate Redox Defense, Angiogenesis, and Immunometabolism for Osteoporotic Bone Regeneration

Yifan Gu[1,2,*], Lei Li[3,*], Yan Shen[4], Yiheng Li[4], Yicong Wang[4], Ziru Wang[4], Kun Wang[4], Shuai Jiang[4], Tinggang Xu[4], Min Yang[5]

[1]Postdoctoral Research Station, The First Affiliated Hospital of Wannan Medical University (Yijishan Hospital of Wannan Medical University), Wuhu, Anhui, People's Republic of China; [2]Postdoctoral Research Station, Medical Integration and Practice Center, Shandong University, Jinan, Shandong, People's Republic of China; [3]Central Laboratory, The First Affiliated Hospital of Wannan Medical University (Yijishan Hospital of Wannan Medical University), Anhui, People's Republic of China; [4]Graduate School, Wannan Medical University, Wuhu, Anhui, People's Republic of China; [5]Department of Trauma Orthopedics, The First Affiliated Hospital of Wannan Medical University (Yijishan Hospital of Wannan Medical University), Wuhu, Anhui, People's Republic of China

*Yifan Gu and Lei Li contributed equally to this work

Correspondence: Min Yang, Email pkuyang@hotmail.com

Purpose: In osteoporotic conditions, bone regeneration is hindered by a pathological triad: persistent oxidative stress, compromised vascularization, and a dysregulated osteoimmune microenvironment. The purpose of this study was to engineer a multifunctional nanotherapeutic platform capable of orchestrating redox defense, angiogenesis, and immunometabolic reprogramming to accelerate bone repair.

Methods: We synthesized a tri-functional nanozyme (MgTA@MnO_2) featuring a metal-phenolic network (MPN) coating, established through the one-step coordination of tannic acid (TA) and magnesium ions (Mg^{2+}) onto manganese dioxide nanoparticles. For sustained local delivery, these catalytic nanomedicines were dispersed within a standard photocrosslinkable, injectable methacrylated gelatin (GelMA) matrix. The system's efficacy was evaluated across pre-osteoblast, endothelial, and macrophage cell models. Underlying immunomodulatory mechanisms were delineated using transcriptomic sequencing. Therapeutic outcomes were assessed in an ovariectomized (OVX) osteoporotic rat model bearing femoral bone defects.

Results: The localized nanozyme delivery system efficiently scavenged reactive oxygen species (ROS), protecting osteoblasts from oxidative damage by awakening the endogenous NRF2 defense pathway. The platform also robustly stimulated endothelial cell migration and tube formation. Crucially, Mg^{2+} and TA synergized with the MnO_2 core to drive precise macrophage reprogramming, shifting the population from a pro-inflammatory M1 state toward a pro-reparative M2 phenotype. Transcriptomic profiling revealed this immunometabolic transition was dictated by targeted suppression of the IL-17/MAPK/NF-κB inflammatory axis and concurrent activation of the STAT3/IL-10 cascade. Consequently, this optimized osteoimmune niche promoted osteogenesis while restraining osteoclastogenesis in vitro. In vivo evaluations confirmed excellent biosafety and demonstrated markedly accelerated, vascularized trabecular bone regeneration, correlating with robust M2 macrophage infiltration.

Conclusion: By coupling catalytic ROS scavenging with targeted immunometabolic modulation, the MgTA@MnO_2 nanotherapeutic system successfully remodels the hostile osteoporotic microenvironment. Utilizing a conventional hydrogel as a local vehicle, this tri-functional nanozyme approach provides a highly translatable paradigm for managing compromised bone fractures.

Keywords: nanomedicine, osteoimmunomodulation, macrophage polarization, metal-phenolic network, magnesium ion delivery, osteoporotic fracture healing

https://doi.org/10.2147/IJN.S606744
Received: 9 March 2026
Accepted: 30 April 2026
Published: 6 May 2026

Introduction

Restoring bone continuity in osteoporotic patients remains a demanding clinical task in orthopedics. [1,2] The difficulty fundamentally stems from the unique pathological microenvironment inherent to osteoporosis, fundamentally disrupting standard tissue repair cascades. Elevated local reactive oxygen species (ROS) induce oxidative stress. This biochemical state causes direct structural and functional damage to osteoblasts.[3,4] Concurrently, restricted local angiogenesis limits the transport of essential nutrients and osteoprogenitor cells to the defect area. [5] Beyond these factors, a dysregulated immune landscape critically undermines bone remodeling. The prolonged accumulation of proinflammatory (M1) macrophages and their continuous release of inflammatory cytokines, including TNF-α and IL-6, severely compromise healing outcomes. [6,7] Regenerative failure in osteoporosis, thus, represents a profound dysfunction of the osteoimmune microenvironment rather than an isolated metabolic deficiency.

Methacrylated gelatin (GelMA) inherently possesses properties such as injectability and tunable photocrosslinking, making it a highly viable candidate matrix for delivering bioactive agents in bone defect repair.[8] Moreover, the intrinsic cross-linked structural properties of GelMA hydrogels endow them with superior sustained-release capabilities, functioning as an optimized localized depot. This allows for the controlled delivery of encapsulated bioactive agents, thereby maintaining therapeutic concentrations at the defect site while effectively minimizing potential systemic toxicity. Unmodified variants of this matrix, while offering good biocompatibility and cell adhesion, typically act as passive structural scaffolds. They lack the functional capacity to actively reverse the complex pathological barriers associated with osteoporosis. Current material design paradigms increasingly involve incorporating multifunctional agents into GelMA to actively intervene in local tissue environments.[9,10] Nanozymes, characterized by their enzyme-mimetic catalytic behaviors, present a versatile engineering option.[11] Manganese dioxide-based nanozymes, for instance, demonstrate robust hydrogen peroxide degradation capabilities that effectively mitigate local oxidative stress.[12] Natural polyphenols such as tannic acid (TA) and specific bioactive metal ions are also frequently utilized to introduce antioxidant, anti-inflammatory, or osteogenic properties into hydrogel networks.[13–16] While these individual modifications are valuable, addressing single pathological elements often proves insufficient for comprehensive healing. Orchestrating multiple bioactive constituents within a unified platform is essential to concurrently resolve the interconnected osteoimmune and metabolic dysfunctions.

Despite these advances, a significant limitation remains. Many current strategies address only one or two pathological barriers in isolation. A biomaterial capable of systemically and coordinately remodeling the entire pathological network —especially the core dysregulated osteoimmune crosstalk—is still needed. Achieving such integrated modulation requires a rational design that orchestrates multiple bioactive components to work in concert.

Directing macrophage phenotypic transitions within this multifunctional framework is heavily recognized as a central determinant of bone repair quality.[17] The timely shift from a proinflammatory M1 state to an anti-inflammatory, pro-reparative M2 state is a prerequisite for initiating effective tissue regeneration.[18,19] Under osteoporotic conditions, macrophages typically fail to undergo this transition. They sustain an inflammatory milieu that halts osteogenesis and accelerates osteoclast activity, creating a persistent cycle that impedes tissue restoration.[7,20] Reprogramming these immune cells serves as a foundational step to reshape the pro-regenerative immune microenvironment and properly rebalance bone metabolism.[21,22]

Integrating immunomodulatory, antioxidant, and pro-angiogenic functions within a cohesive hydrogel platform remains a significant technical hurdle for coordinating the osteoporotic microenvironment. Strategic selection of bioactive components is essential to achieve this. Magnesium ions (Mg^{2+}) act as vital bone minerals that directly stimulate osteoblast and endothelial cell activities.[23,24] Emerging evidence also suggests their capacity to favor macrophage polarization toward a pro-reparative phenotype.[25] Combining Mg^{2+} with the ROS-scavenging properties of an MnO_2 core and the metal-chelating, antioxidant abilities of TA create a highly synergistic formulation. This specific triad targets the primary obstacles of osteoporotic healing: oxidative stress, restricted vascularization, and immune imbalance. The hypothesis that embedding these elements into a single matrix can actively reprogram the osteoimmune microenvironment to drive functional bone regeneration requires rigorous validation.

Guided by this framework, we engineered a MgTA@MnO_2/GelMA composite hydrogel. A straightforward one-step in-situ coordination strategy was utilized to synthesize MgTA@MnO_2 nanozymes, which were subsequently embedded into the GelMA network. We hypothesized that this system would promote osteoporotic bone regeneration through integrated mechanisms: (1) Antioxidant Protection: The MnO_2 core and TA components are intended to neutralize ROS, safeguarding osteoblasts and engaging endogenous cellular antioxidant pathways. (2) Pro-angiogenic Effect: Mg^{2+} paired with an optimized local microenvironment is expected to enhance endothelial cell function and facilitate vascularization. (3) Core Immunomodulation: The coordinated actions of Mg^{2+} and TA within the metal-phenolic network aim to modulate macrophage polarization toward the M2 phenotype, restructuring the osteoimmune environment to favor osteogenesis while suppressing osteoclastogenesis. We performed comprehensive material characterization, in vitro validation of cellular functions, transcriptomic pathway analysis of macrophage reprogramming, and in vivo evaluation using an osteoporotic rat bone defect model to rigorously test this system. Scheme 1 summarizes the overall design strategy and conceptual framework.

Materials and Methods

Synthesis of MgTA@MnO_2 Nanozymes

MgTA@MnO_2 nanozymes were fabricated via a one-step in situ coordination strategy. Briefly, 80 mg of commercial manganese dioxide nanoparticles (~100 nm; Macklin, #M902394) were dispersed in 80 mL of Tris-HCl buffer (20 mM, pH 7.4; Beyotime, #ST774) and homogenized via ultrasonication (150 W). Separately, an equal volume (80 mL) of an aqueous mixture containing 0.1 M tannic acid (TA; Macklin, #T818845) and 0.1 M $MgSO_4 \cdot 7H_2O$ (Macklin, #M885229) was prepared. This TA-Mg^{2+} mixture was then added dropwise to the MnO_2 suspension under vigorous magnetic stirring (1000 rpm). The reaction proceeded overnight at 37 °C, facilitating the spontaneous self-assembly of a highly stable metal-phenolic network (MPN) coating onto the MnO_2 surfaces. The resulting MgTA@MnO_2 nanozymes were collected by centrifugation, washed repeatedly with deionized water to remove any unreacted precursors, and lyophilized at −80 °C for 48 h. Unmodified MnO_2 and TA@MnO_2 (prepared without Mg^{2+}) were synthesized under identical conditions as controls.

Physicochemical Characterization

The morphology and size distribution of nanozymes were observed via transmission electron microscopy (TEM; FEI Tecnai G2 F20). X-ray photoelectron spectroscopy (XPS; Thermo Scientific K-Alpha) was performed to analyze the surface elemental composition and chemical states of the nanoparticles, with all spectra calibrated to the C 1s peak at 284.8 eV. Fourier-transform infrared (FTIR) spectra were recorded in attenuated total reflectance (ATR) mode from 400 to 4000 cm^{-1} (Thermo Scientific Nicolet iS20) to identify characteristic functional groups of the composites. The hydrodynamic diameter and zeta potential of nanoparticles were measured via dynamic and electrophoretic light scattering using a Malvern Zetasizer Pro.

In Vitro Release Kinetics of Nanozymes

To evaluate the environment-responsive degradation and release behavior, 10 mg of the lyophilized MgTA@MnO_2 nanozymes were sealed in dialysis bags (molecular weight cutoff: 3500 Da) and immersed in 10 mL of release media to simulate different biological conditions. The media included a standard physiological buffer (PBS, pH 7.4) and a simulated osteoporotic pathological microenvironment (pH 6.5, containing 100 μM H_2O_2). The systems were maintained in a constant temperature shaker at 37 °C with gentle agitation. At predetermined time intervals (1, 3, 5, 7, 10, and 14 days), 1 mL of the external release medium was collected for analysis, and an equal volume of fresh corresponding buffer was immediately replenished. The concentrations of released Mg and Mn ions were precisely quantified using Inductively Coupled Plasma Optical Emission Spectrometry (ICP-OES). Concurrently, the release of TA was determined by measuring the absorbance at 273 nm via UV-Vis spectrophotometry. All release experiments were performed in independent triplicates.

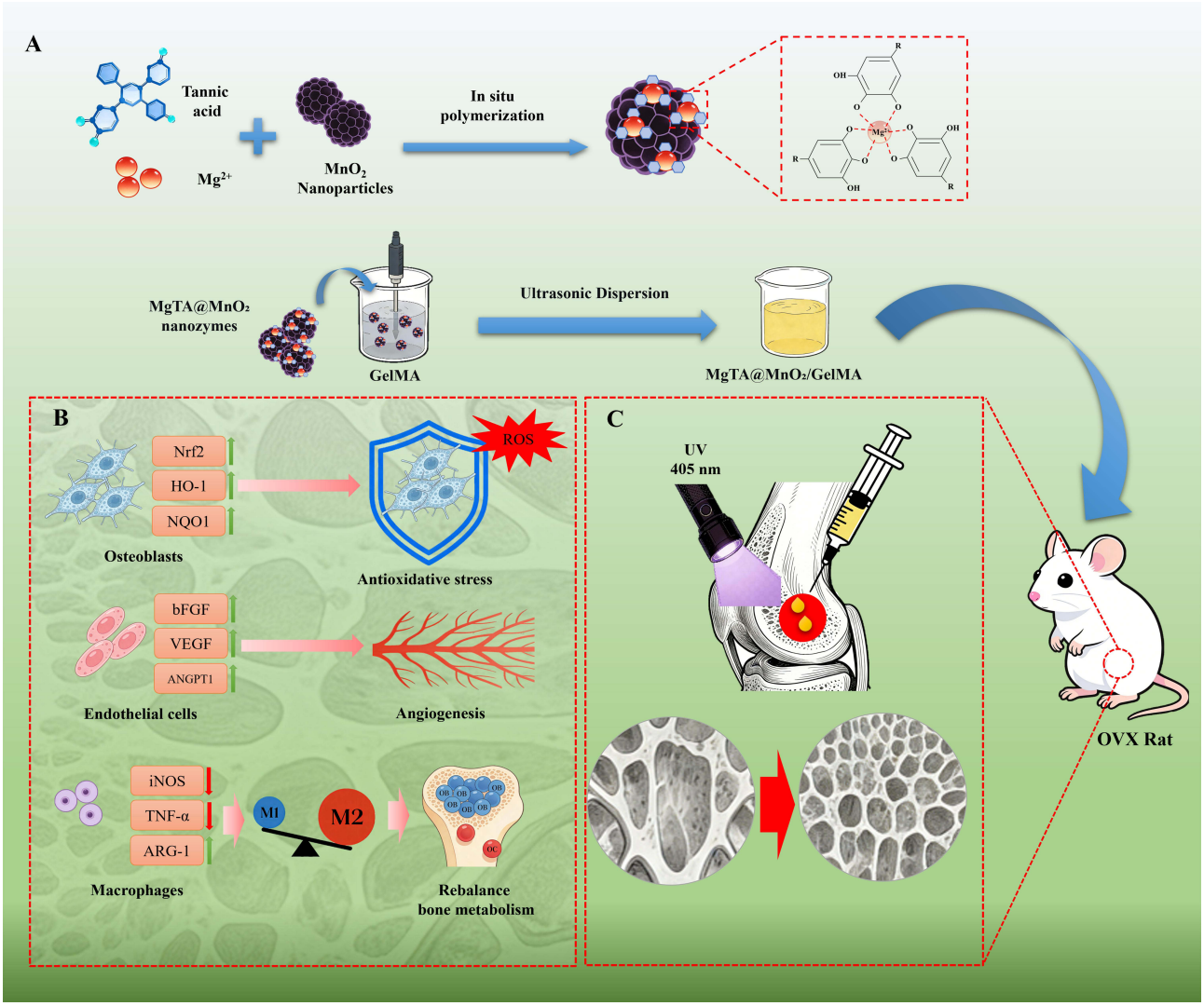

Scheme 1 Fabrication of the multifunctional MgTA@MnO_2/GelMA composite hydrogel and its integrated strategy for promoting osteoporotic bone repair via an immunomodulatory core mechanism. **(A)** The MgTA@MnO_2 nanozyme was synthesized via a one-step in-situ coordination method, in which tannic acid (TA) and magnesium ions (Mg^{2+}) were co-modified on the surface of manganese dioxide (MnO_2) sheet-like nanoparticles. The resulting nanozyme was then uniformly dispersed in a methacrylated gelatin (GelMA) precursor solution, followed by UV (405 nm) cross-linking to obtain an injectable composite hydrogel. **(B)** In vitro, the hydrogel exhibits multiple biological functions, including scavenging reactive oxygen species (ROS) and activating the NRF2/HO-1/NQO1 antioxidant pathway in osteoblasts, promoting endothelial cells to express angiogenic factors (bFGF, VEGF, ANGPT1) to enhance vascularization, and critically reprogramming macrophages from a pro-inflammatory M1 phenotype (iNOS$^+$, TNF-α$^+$) to a pro-reparative M2 phenotype (ARG-1$^+$). This collective action modulates the osteoimmune microenvironment and rebalances bone metabolism. **(C)** In an ovariectomized (OVX) osteoporotic rat model with bone defects, the hydrogel effectively promotes new bone formation and achieves significant bone repair through the synergistic effects described above. (Upward arrows (↑) and downward arrows (↓) indicate upregulation/increase and downregulation/decrease, respectively).

Fabrication and Characterization of Composite Hydrogels

A prepolymer solution was prepared by dissolving 5% (w/v) methacrylated gelatin (GelMA; EFL, #EFL-GM60) and 0.25% (w/v) the photoinitiator lithium phenyl-2,4,6-trimethylbenzoylphosphinate (LAP; EFL, #EFL-LAP) in phosphate-buffered saline (PBS; Servicebio, #G4202), leveraging the inherent injectability of the GelMA matrix as a local delivery vehicle. MgTA@MnO_2 nanozymes (final concentration: 1.00% w/v) were added to the prepolymer solution and dispersed uniformly via probe ultrasonication (100 W, 5 min, 2s on/3s off cycle in an ice bath) to prevent local overheating. The mixture was then exposed to 405 nm UV light to induce photocrosslinking, forming the MgTA@MnO_2/GelMA composite hydrogels. Pure GelMA hydrogels and MnO_2-loaded GelMA hydrogels were prepared via the same procedure as controls.

The internal porous microstructure of freeze-dried hydrogels was examined using scanning electron microscopy (SEM; ZEISS GeminiSEM 300). The compressive mechanical properties of hydrogels were assessed using a universal testing machine (Instron 5943). The H_2O_2 decomposition activity of the composite hydrogels was evaluated via a standard titanium sulfate colorimetric assay, using H_2O_2 (Macklin, #H792077) and $Ti(SO_4)_2$ (Macklin, #T822549) as reaction substrates.

Cell Culture

Three cell lines were used for in vitro experiments: murine pre-osteoblast MC3T3-E1 cells (BDBIO, #C5102), murine RAW 264.7 monocyte/macrophage cells (BDBIO, #C5142), and human umbilical vein endothelial cells (HUVECs; BDBIO, #C6551). MC3T3-E1 cells were cultured in α-MEM (BDBIO, #L105500), RAW 264.7 cells in high-glucose DMEM (BDBIO, #L100500), and HUVECs in endothelial cell growth medium (BDBIO, #C6551500). All culture media were supplemented with 10% fetal bovine serum (BDBIO, #F800500) and 1% penicillin-streptomycin solution (BDBIO, #A200100). Cells were maintained in a humidified incubator at 37 °C with 5% CO_2, with medium refreshed every 2–3 days. All cell lines were originally sourced from the Cell Bank of the Chinese Academy of Sciences (Shanghai, China).

Biocompatibility and Antioxidant Assays

The cytocompatibility of the hydrogels was evaluated using the Cell Counting Kit-8 (CCK-8; Beyotime, #C0037). To determine the optimal nanozyme loading concentration, composite hydrogels incorporated with varying mass fractions of MgTA@MnO_2 (0.125%, 0.25%, 0.50%, 1.00%, and 2.00%, w/v) were prepared. Hydrogel extracts were obtained by incubating these samples in complete cell culture medium at a mass-to-volume ratio of 0.1 g/mL for 24 h at 37 °C, according to ISO 10993–12 standards. The resulting supernatants were collected and sterilized through a 0.22 μm filter. MC3T3-E1 cells were subsequently cultured with these extracts for 24, 48, and 72 h. Based on the CCK-8 screening results, the optimal formulation was selected for all subsequent biological experiments. Cell viability was further visualized via live/dead staining (Calcein-AM/PI kit; Beyotime, #C2015M). For antioxidant functional assessments, MC3T3-E1 cells were pre-treated with the optimized hydrogel extract and then exposed to 200 μM H_2O_2 for 24 h to establish an in vitro oxidative stress model. Intracellular reactive oxygen species (ROS) levels were detected utilizing the DCFH-DA probe (Beyotime, #S0035S). Briefly, cells were incubated with 10 μM DCFH-DA at 37 °C for 20 min in the dark and subsequently washed three times with serum-free medium, followed by quantitative flow cytometry and qualitative fluorescence microscopy. Variations in mitochondrial membrane potential were tracked using a JC-1 staining kit (Beyotime, #C2006). According to the manufacturer's protocol, cells were incubated with the JC-1 working solution at 37 °C for 20 min in the dark, washed twice with the provided JC-1 buffer, and immediately observed under a fluorescence microscope. The protein expression levels of key antioxidant pathway molecules, specifically NRF2, HO-1, and NQO1, were quantified by Western blotting. Detailed antibody specifications are provided in Supplementary Table 1.

Angiogenesis Assays

The pro-angiogenic capacity of the composite hydrogels was evaluated using HUVECs cultured in conditioned media from different hydrogel groups (utilized at a 100% extract concentration, derived strictly according to the 0.1 g/mL standard extraction protocol). For the tube formation assay, HUVECs were seeded onto Growth Factor Reduced Matrigel (Corning, #356234), and network parameters (branch point number, total tube length) were quantified after 6 h of incubation. The migratory capacity of HUVECs was assessed via a standard scratch wound healing assay, with images captured at 0, 24, and 48 h post-scratching. The protein expression of key pro-angiogenic factors (VEGF, bFGF, Angiopoietin-1) was detected via Western blot, with antibody details provided in Supplementary Table 1.

Macrophage Polarization Assays

RAW 264.7 macrophages were stimulated with LPS (100 ng/mL; MCE, #HY-D1056) for M1 polarization or IL-4 (20 ng/mL; MCE, #HY-P7080) for M2 polarization, with concurrent treatment of hydrogel extracts. Macrophage phenotypic transition was evaluated via two approaches: immunofluorescence co-staining of M1 surface marker CD86 and M2

surface marker CD206, and Western blot analysis of classical polarization markers (iNOS, TNF-α for M1 phenotype; ARG-1 for M2 phenotype). Antibody specifications are detailed in Supplementary Tables 1 and 2.

Transcriptomics and Signaling Pathway Analysis

Total RNA was extracted from RAW 264.7 cells assigned to two groups: LPS stimulation alone, and LPS stimulation combined with MgTA@MnO_2/GelMA hydrogel extract treatment, using TRIzol reagent (Servicebio, #G3013). RNA sequencing and bioinformatic analyses, including differentially expressed gene (DEG) screening, Gene Ontology (GO) enrichment, and Kyoto Encyclopedia of Genes and Genomes (KEGG) pathway annotation, were performed by Tsingke Biotechnology Co., Ltd. Core inflammatory signaling pathways identified via sequencing (IL-17, MAPK, NF-κB, STAT3) were validated via Western blot, with targeted proteins including p-ERK1/2, p-NF-κB p65, p-STAT3, IL-17A, and IL-10. Antibody information is available in Supplementary Table 1.

Osteogenesis and Osteoclastogenesis Modulation

Conditioned media (CM) were collected from macrophages with different polarization treatments. The concentrations of key inflammatory and anti-inflammatory cytokines (IL-17A, TNF-α, IL-6, IL-10; Boster) in CM were quantified via enzyme-linked immunosorbent assay (ELISA).

For osteogenic differentiation assessment, MC3T3-E1 cells were cultured in osteogenic induction medium (BDBIO, #G4119) supplemented with the corresponding CM. Osteogenic differentiation was evaluated via alkaline phosphatase (ALP) staining (Beyotime, #C3206) after 7 days of induction. Briefly, cells were fixed with 4% paraformaldehyde for 15 min, washed, and incubated with the BCIP/NBT working solution at room temperature for 30 min in the dark. For extracellular matrix mineralization, Alizarin Red S (ARS) staining (Beyotime, #C0148S) was conducted after 14 days of induction. The fixed cells were stained with 1% Alizarin Red S solution at room temperature for 30 min and then thoroughly washed with distilled water. In parallel, quantitative real-time PCR (qRT-PCR) for osteogenic marker genes (Runx2, ALP, OSX, BMP2) was performed.

For osteoclastogenesis evaluation, RAW 264.7 cells were cultured in CM supplemented with RANKL (50 ng/mL; PeproTech). After 5 days of induction, osteoclastic differentiation was assessed via tartrate-resistant acid phosphatase (TRAP) staining (Bestbio, #BB-4421). Briefly, the cells were fixed and incubated with the TRAP working solution at 37 °C for 1 h in the dark, followed by observation under a light microscope. In parallel, qRT-PCR for osteoclast-specific genes (NFATc1, CTSK, TRAP, c-Fos) was performed. Primer sequences are listed in Supplementary Table 3.

In vivo Osteoporotic Bone Defect Model

All animal experimental protocols were reviewed and approved by the Animal Welfare and Ethics Committee of Wannan Medical University (approval No. WNMC-AWE-2025323). All procedures were performed in strict accordance with the National Institutes of Health Guide for the Care and Use of Laboratory Animals. All surgical procedures, including the bilateral ovariectomy (OVX) and the subsequent bone defect creation, were performed under general anesthesia via intraperitoneal injection of sodium pentobarbital (50 mg/kg body weight) to minimize animal suffering. Postoperative analgesia (subcutaneous injection of buprenorphine, 0.05 mg/kg) was administered for three consecutive days to alleviate pain.

Osteoporosis was induced in 3-month-old female Sprague-Dawley rats via bilateral ovariectomy (OVX). Eight weeks after OVX surgery, a cylindrical defect (2.0 mm diameter, 3.0 mm depth) was drilled in the distal femoral condyle of each rat. Animals were randomly allocated into three groups (n = 6 per group at each time point): blank control group (defect left untreated), GelMA hydrogel group, and MgTA@MnO_2/GelMA hydrogel group. In the treatment groups, the hydrogel precursor (containing 1.00% w/v MgTA@MnO_2) was first pre-crosslinked under 405 nm UV light for 14s to reach an injectable state. Approximately 10 μL of the pre-crosslinked hydrogel was then injected into each defect and further crosslinked in situ for an additional 30s to ensure complete stabilization within the host bone. Femur samples were harvested at 4, 8, and 12 weeks post-implantation for subsequent analysis. At the designated experimental endpoints, all animals were humanely euthanized via an intraperitoneal injection of an overdose of sodium pentobarbital

(150 mg/kg). This euthanasia procedure was carried out in strict compliance with the American Veterinary Medical Association (AVMA) Guidelines for the Euthanasia of Animals.

Histomorphometric and Biosafety Evaluation

Harvested femur samples were fixed and scanned via micro-computed tomography (micro-CT; Bruker SkyScan 1276). Quantitative bone morphometric analysis was performed within the predefined region of interest (ROI) covering the entire defect area, with core parameters including bone mineral density (BMD), bone volume/total volume ratio (BV/TV), trabecular number (Tb.N), and trabecular separation (Tb.Sp). After decalcification, samples were embedded, sectioned, and stained with Hematoxylin & Eosin (H&E) and Masson's trichrome for histological evaluation. Immunofluorescence staining was performed on serial sections to detect CD68 (M1 macrophages), CD163 (M2 macrophages), VEGF, and Osterix (OSX). The detailed specifications of the primary antibodies used for these evaluations are listed in Supplementary Table 2. For systemic biosafety assessment, major organs (heart, liver, spleen, lung, and kidney) were harvested, sectioned, and stained with H&E for histopathological examination. These sections were independently evaluated by a professional pathologist blinded to the experimental groupings. Assessment criteria focused on identifying markers of acute or chronic toxicity, including cellular necrosis, inflammatory cell infiltration, structural tissue disorder, and microvascular congestion.

Statistical Analysis

Data are expressed as mean ± SD. Statistical analyses were performed in GraphPad Prism 9.0. Two-group comparisons used two-tailed Student's *t*-test. Single-timepoint multi-group comparisons were analyzed by one-way ANOVA with Tukey's post-hoc test. Longitudinal in vivo repeated measurements were assessed via two-way repeated measures ANOVA with Tukey's post-hoc test. Significance was set at $p < 0.05$.

Results

Construction of the MgTA@MnO_2 Nanozymes

MgTA@MnO_2 nanozymes were successfully synthesized utilizing a streamlined in situ coordination methodology. This procedure involved co-assembling natural polyphenolic tannic acid (TA) and bioactive magnesium ions (Mg^{2+}) onto the functional surfaces of manganese dioxide (MnO_2) sheet-like nanoparticles (Figure 1A). Transmission electron microscopy (TEM) imaging confirmed that the native sheet-like morphology remained uniform and structurally intact following this sequential modification (Figure 1B). Subsequent X-ray photoelectron spectroscopy (XPS) positively identified the integrated presence of Mn, O, C, and Mg elements (Figure 1C). Furthermore, Fourier transform infrared (FTIR) spectroscopy was employed to delineate the chemical structure and verify the successful functionalization of the MgTA@MnO_2 nanozymes (Figure 1D). The characteristic broad absorption band spanning ~500-600 cm^{-1} is primarily attributed to the Mn-O vibrations of the core. The successful coating of tannic acid is confirmed by the distinct peaks at ~1710 cm^{-1} and ~1600 cm^{-1}, corresponding to the C=O and aromatic C=C stretching vibrations, respectively. Crucially, upon the integration of Mg^{2+}, specific spectral perturbations—notably the subtle peak shifts and relative intensity alterations in the 1300–1400 cm^{-1} region (phenolic C-O stretching) and at ~1710 cm^{-1}—were observed when compared to the TA@MnO_2 spectrum. These localized spectral changes provide explicit evidence for the successful metallophenolic coordination between Mg^{2+} and TA on the MnO_2 surface, confirming the formation of an integrated multicomponent network. Finally, dynamic light scattering (DLS) alongside zeta potential measurements demonstrated a distinct surface charge shift, while the particles maintained a homogeneous hydrodynamic size distribution following the metal-phenolic network (MPN) coating process (Figure 1E and F).

Furthermore, the stimuli-responsive degradation and release kinetics of the MgTA@MnO_2 nanozymes were investigated in vitro. As shown in Supplementary Figure S1, the nanozymes exhibited exceptional stability under physiological conditions (pH 7.4), demonstrating minimal ion leakage over the 14-day observation period. In stark contrast, within a simulated osteoporotic pathological microenvironment (pH 6.5 containing 100 μM H_2O_2), the nanozymes underwent rapid responsive degradation within the first 3 days, followed by a sustained release plateau. Importantly, this

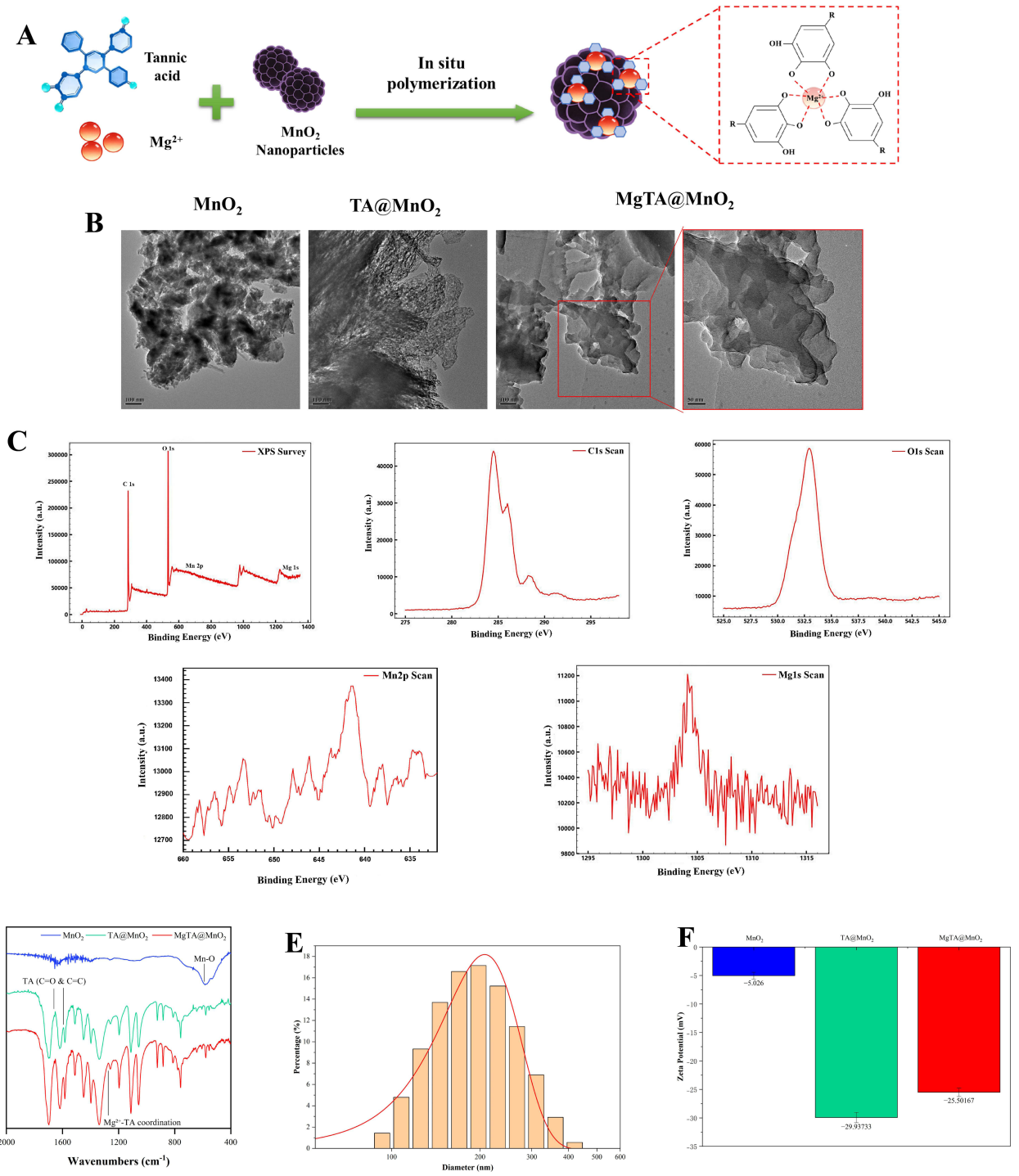

Figure 1 Characterization of MgTA@MnO_2 nanozymes. (**A**) Schematic illustration of the one-step synthesis of MgTA@MnO_2 nanozymes via in-situ coordination, where TA and Mg^{2+} are grafted onto MnO_2 sheet-like nanoparticles. (**B**) Transmission electron microscopy (TEM) images of MnO_2, TA@MnO_2, and MgTA@MnO_2. (**C**) X-ray photoelectron spectroscopy (XPS) analysis of MgTA@MnO_2 nanozymes. (**D**) Fourier transform infrared (FTIR) spectra. (**E**) Dynamic light scattering (DLS) profile showing the hydrodynamic size distribution. (**F**) Zeta potential analysis.

intelligent, on-demand degradation restricts the release of Mg^{2+} and Mn^{2+} to a biologically safe and effective trace level. This microenvironment-responsive trait ensures a sustained supply of bioactive metal cofactors to activate downstream reparative pathways, while perfectly circumventing the localized burst-release toxicity typically associated with traditional biodegradable metal materials.

https://doi.org/10.2147/IJN.S606744

Formulation and Physicochemical Properties of the Composite Hydrogel

The synthesized MgTA@MnO_2 nanozymes were uniformly dispersed into an aqueous methacrylated gelatin (GelMA) precursor solution. Upon exposure to targeted UV irradiation (405 nm), this fluidic precursor rapidly underwent photo-crosslinking to form a stable, shape-adaptable 3D hydrogel matrix (Figure 2A–C). Scanning electron microscopy (SEM) coupled with energy-dispersive X-ray spectroscopy (EDS) mapping confirmed the interconnected porous microarchitecture of the hydrogel and verified the thoroughly homogeneous spatial distribution of the nanozymes (evidenced by the overlapping Mn, Mg, C, and O signals) within the matrix (Figure 2D). Furthermore, compressive stress–strain analyses elucidated that the dynamic coordination between TA and Mg^{2+} effectively mitigated the mechanical deterioration typically associated with raw nanoparticle incorporation, thereby reinforcing the overall structural integrity of the composite network (Figure 2E). Functionally, the integrated hydrogel platform exhibited robust catalase-mimetic catalytic activity, demonstrating sustained and ROS-responsive H_2O_2 decomposition kinetics in an in vitro setting (Figure 2F).

Restoration of Intracellular Redox Homeostasis and NRF2 Pathway Activation

Initially, the cytocompatibility of the MgTA@MnO_2/GelMA hydrogel was confirmed via standard CCK-8 assays and live/dead fluorescence staining. The composite matrix demonstrated excellent biocompatibility, sustaining high viability and continuously promoting the proliferation of MC3T3-E1 pre-osteoblasts (Figure 3A–C). To evaluate its cytoprotective efficacy against oxidative damage, an in vitro H_2O_2-induced oxidative stress model was established. Both quantitative flow cytometry and qualitative DCFH-DA fluorescence imaging revealed that treatment with the hydrogel extract significantly attenuated intracellular reactive oxygen species (ROS) accumulation (Figure 3D, E, G). Furthermore, JC-1 staining demonstrated the robust preservation of the mitochondrial membrane potential, effectively protecting the pre-osteoblasts from oxidative-induced mitochondrial dysfunction (Figure 3F, H, I). To elucidate the underlying molecular mechanisms driving this cytoprotection, the expression of key antioxidant proteins was quantified via Western blotting. The hydrogel intervention markedly upregulated the master transcription factor NRF2, along with its downstream effectors HO-1 and NQO1. This indicates that beyond simply acting as an extracellular ROS scavenger, the integrated nanozyme platform actively engages and amplifies the endogenous cellular antioxidant defense cascade (Figure 3J–M).

Pro-Angiogenic Effects in vitro

The in vitro pro-angiogenic capacity of the composite hydrogel platform was rigorously evaluated utilizing human umbilical vein endothelial cells (HUVECs). In standard scratch wound-healing assays, conditioned medium derived from the MgTA@MnO_2/GelMA hydrogel significantly enhanced endothelial cell migration and accelerated the wound closure rate compared to the control groups (Figure 4A and B). Concurrently, when HUVECs were seeded on Matrigel substrates, this specialized medium promoted the robust spatial organization of capillary-like tube formation, evidenced by the quantitative increases in both the number of branch points and the total tube length (Figure 4C–E). To elucidate the molecular basis of this enhanced angiogenic response, the expression of key functional proteins was assessed via Western blotting. The analysis revealed a pronounced upregulation of essential pro-angiogenic factors—specifically basic fibroblast growth factor (bFGF), vascular endothelial growth factor (VEGF), and Angiopoietin-1—within the hydrogel-treated cells (Figure 4F–I). These findings collectively demonstrate that the MgTA@MnO_2/GelMA platform fosters a highly favorable microenvironment for neo-vascularization, which serves as a critical prerequisite for subsequent bone tissue regeneration.

Macrophage Reprogramming Toward a Pro-Reparative M2 Phenotype

The immunomodulatory capacity of the composite hydrogel was systematically evaluated utilizing an in vitro LPS-induced RAW264.7 macrophage inflammation model. To accurately track the phenotypic transition, both immunofluorescence staining and Western blot analyses were conducted. Compared to the hyper-inflammatory state of the LPS-only control group, intervention with the MgTA@MnO_2/GelMA hydrogel significantly mitigated the expression of M1-associated pro-inflammatory markers. Specifically, immunofluorescence imaging demonstrated a pronounced reduction

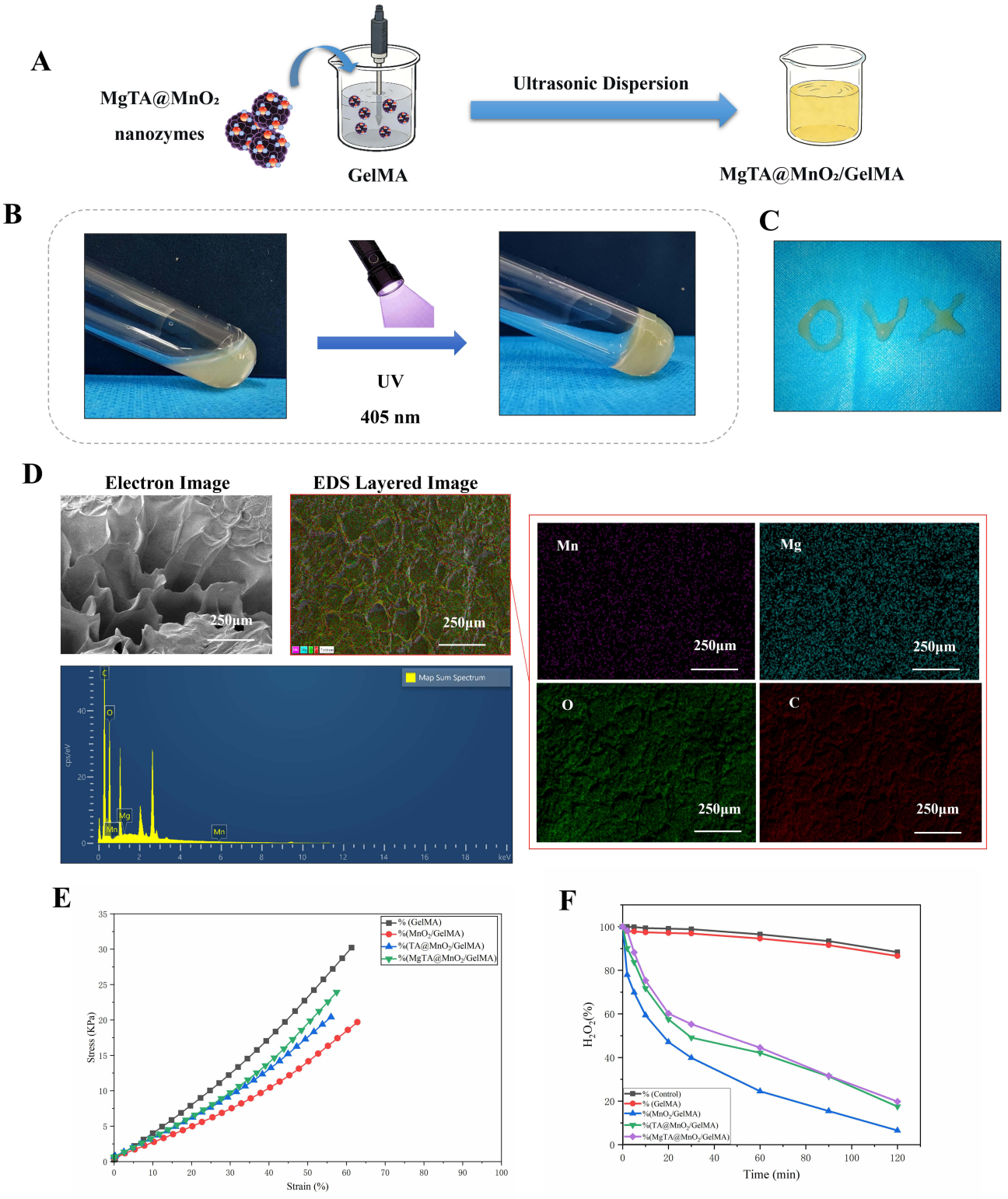

Figure 2 Physicochemical characterization of the MgTA@MnO_2/GelMA composite hydrogel. (**A**) Schematic illustration of the formulation of the MgTA@MnO_2/GelMA hydrogel precursor. (**B**) UV-mediated photocrosslinking (405 nm) of the precursor into a stable hydrogel network. (**C**) Macroscopic evaluation demonstrating the shape-adaptability and potential for localized administration. (**D**) Representative SEM image and corresponding EDS elemental mapping (Mn, Mg, C, and (O) revealing the micro-morphology and homogeneous elemental distribution within the hydrogel matrix. (**E**) Compressive stress–strain curves characterizing the mechanical properties of the composite hydrogels. (**F**) ROS-responsive degradation behavior of the hydrogels in the presence of H_2O_2.

https://doi.org/10.2147/IJN.S606744

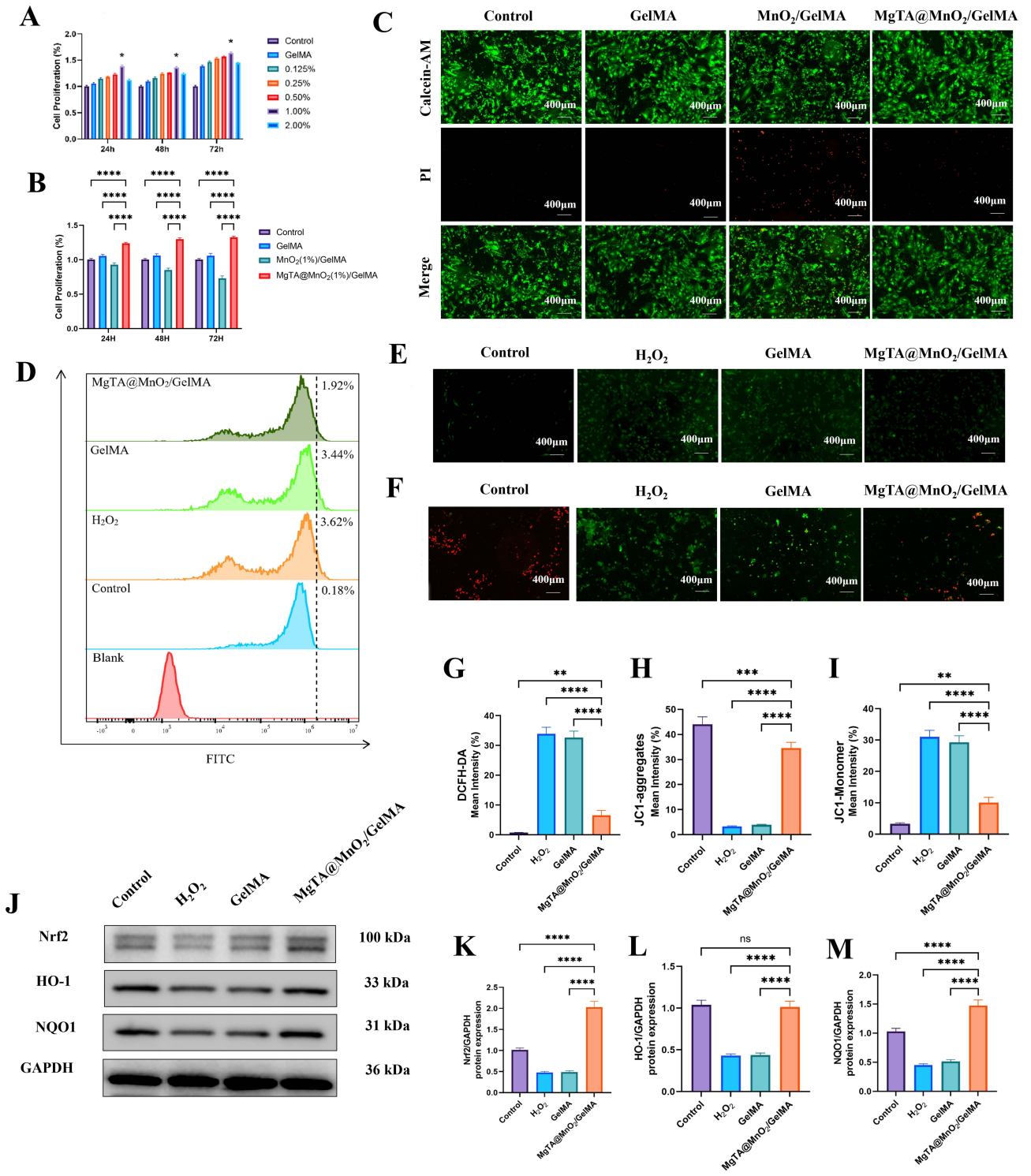

Figure 3 Cytoprotective and antioxidant effects of the MgTA@MnO_2/GelMA hydrogel on MC3T3-E1 pre-osteoblasts under oxidative stress. (**A**) Cell viability assessed via CCK-8 assay following culture with varying concentrations of the hydrogel extract. (**B**) Relative proliferation rates of cells cultured with extracts derived from different hydrogel formulations. (**C**) Representative live/dead fluorescence staining images (green: live cells; red: dead cells). (**D**) Quantitative flow cytometry analysis demonstrating the intracellular ROS-scavenging efficacy. (**E**) Intracellular oxidative stress reduction monitored by DCFH-DA fluorescence imaging across different treatment groups. (**F**) Evaluation of mitochondrial membrane potential variations via JC-1 fluorescence (red fluorescence indicates polarized mitochondria with JC-1 aggregates; green fluorescence indicates depolarized mitochondria with JC-1 monomers). (**G**) Semi-quantitative analysis of intracellular ROS fluorescence intensity. (**H** and **I**) Semi-quantitative evaluation of the JC-1 red/green fluorescence ratio, reflecting mitochondrial membrane potential restoration. (**J–M**) Representative Western blot images and corresponding quantitative analyses of the NRF2, HO-1, and NQO1 antioxidant pathway protein expression levels. Data are presented as mean ± SD (n = 3). *P < 0.05, **P < 0.01, ***P < 0.001, ****P < 0.0001; ns indicates not significant.

https://doi.org/10.2147/IJN.S606744

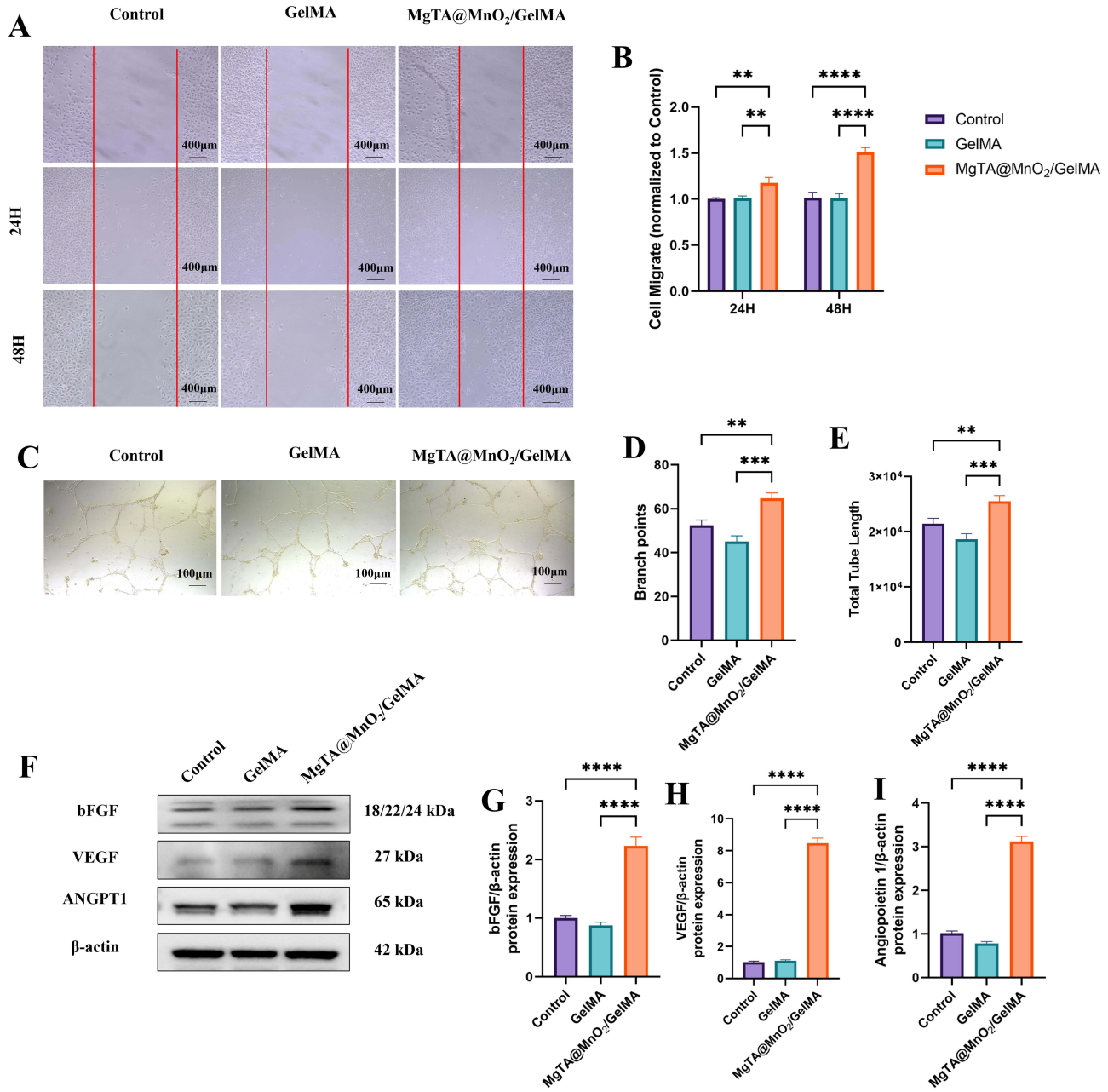

Figure 4 The MgTA@MnO_2/GelMA composite hydrogel enhances the in vitro angiogenic capacity of HUVECs. (**A**) Representative bright-field images of the endothelial scratch wound healing assay at designated time points. The red straight lines indicate the initial wound boundaries. (**B**) Quantitative analysis of the wound closure rate over time. (**C**) Representative optical images of capillary-like tube formation by HUVECs cultured on Matrigel. (**D** and **E**) Quantitative evaluation of the tube formation assay, specifically detailing the number of branch points and total tube length. (**F–I**) Representative Western blot images (F) and corresponding quantitative densitometric analyses (G–I) of the pro-angiogenic proteins bFGF, VEGF, and Angiopoietin-1. Data are presented as mean ± SD (n = 3). **P < 0.01, ***P < 0.001, ****P < 0.0001.

in the M1 surface receptor CD86, which was directly corroborated by the marked downregulation of intracellular iNOS and TNF-α protein expression (Figure 5A, B and D–F). Concomitant with this inflammatory suppression, the hydrogel microenvironment robustly upregulated the expression of M2-associated reparative markers. The treated macrophages exhibited intensified CD206 fluorescence signaling alongside elevated ARG-1 protein levels, mirroring the pro-reparative phenotype typically induced by IL-4 (Figure 5A, C and G, H). Collectively, these phenotypic marker transitions confirm that the integrated platform actively reprograms the macrophage polarization trajectory, effectively converting a hostile inflammatory milieu into a pro-regenerative state.

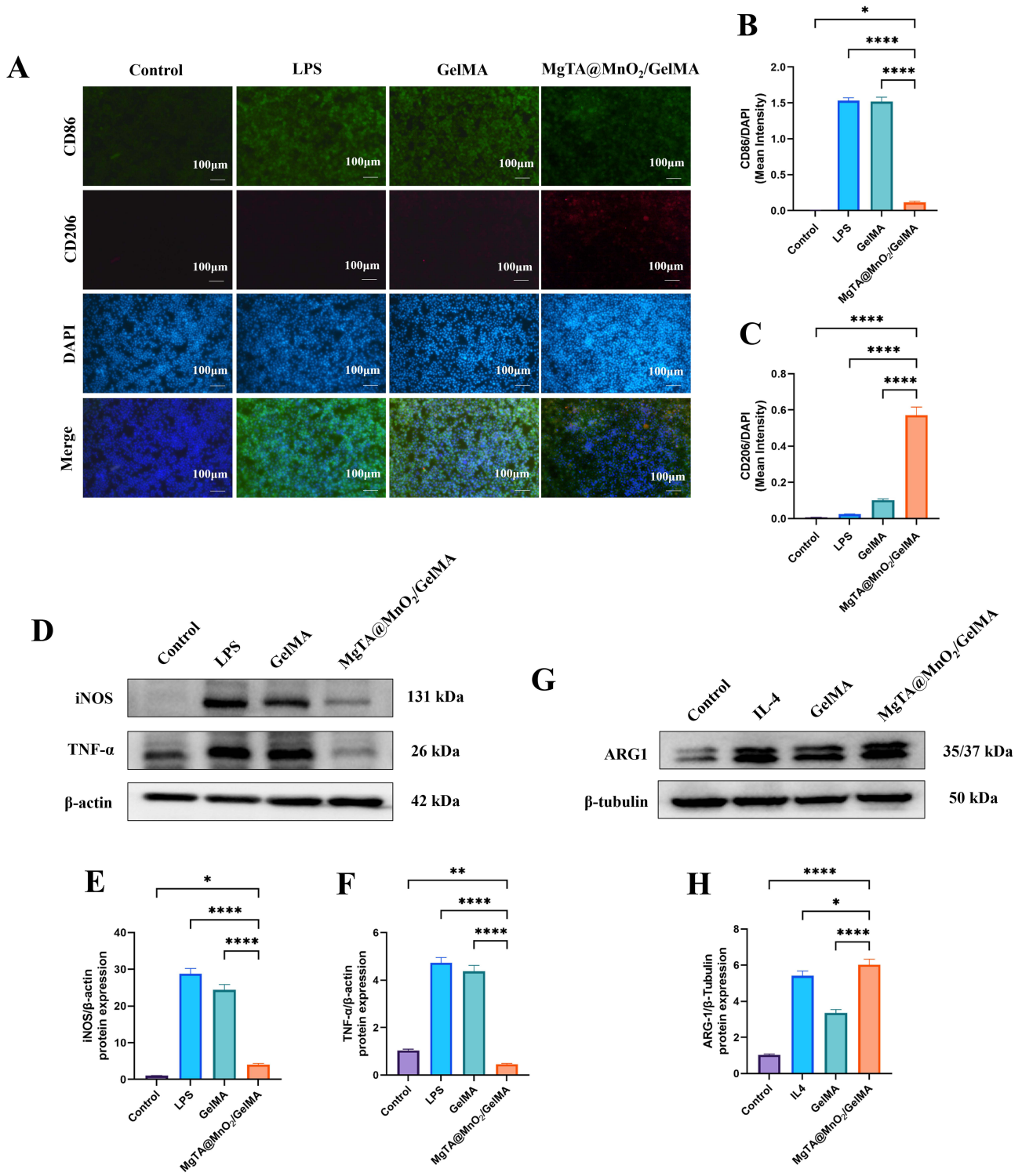

Figure 5 Immunomodulatory effects of the MgTA@MnO_2/GelMA composite hydrogel on RAW264.7 macrophage polarization. (**A**) Representative immunofluorescence double-staining images demonstrating the macrophage phenotypic transition. Compared to the LPS-stimulated group, hydrogel treatment significantly attenuated the expression of the pro-inflammatory M1 marker CD86 (green) while upregulating the tissue-reparative M2 marker CD206 (red). Nuclei were counterstained with DAPI (blue). (**B** and **C**) Semi-quantitative evaluation of CD86 and CD206 fluorescence intensities, normalized to DAPI. (**D–F**) Representative Western blot images (D) and corresponding densitometric quantification (E and F) of the M1-related markers (iNOS, TNF-α) following LPS induction. (**G** and **H**) Representative Western blot images (**G**) and corresponding densitometric quantification (H) of the M2-related marker ARG-1 following IL-4 induction. Data are presented as mean ± SD (n = 3). *P < 0.05, **P < 0.01, ****P < 0.0001.

https://doi.org/10.2147/IJN.S606744

Transcriptomic Profiling and Mechanistic Validation of the IL-17/MAPK/NF-κB Axis

To elucidate the underlying molecular mechanisms driving the observed macrophage reprogramming, RNA sequencing (RNA-seq) was performed. Analysis of the differentially expressed genes (DEGs) revealed distinctly divergent transcriptional profiles between the LPS-stimulated control and the MgTA@MnO_2/GelMA-treated groups (Figure 6A and B). Subsequent Gene Ontology (GO) enrichment analysis indicated that these DEGs were heavily implicated in intracellular signal transduction and inflammatory immune responses (Figure 6C). Crucially, Kyoto Encyclopedia of Genes and Genomes (KEGG) pathway analysis highlighted a profound enrichment in immune-related networks, specifically pinpointing the IL-17 and MAPK signaling cascades as the primary regulatory targets (Figure 6D).

To definitively validate these transcriptomic findings at the translational level, Western blot analysis was conducted. The results confirmed that the composite hydrogel treatment substantially suppressed the LPS-induced hyperactivation of the IL-17A/MAPK/NF-κB inflammatory axis, evidenced by the marked downregulation of IL-17A and the diminished phosphorylation of ERK1/2 (p-ERK1/2) and NF-κB p65 (p-p65). Concurrently, the treatment promoted the activation of the anti-inflammatory STAT3/IL-10 signaling axis. To establish a definitive causal link, a rescue experiment was performed using exogenous recombinant IL-17A protein. The deliberate introduction of IL-17A significantly reversed the hydrogel-mediated immunomodulatory effects and reactivated the downstream inflammatory kinases, unequivocally confirming the targeted blockade of the IL-17A signaling cascade as the core mechanistic driver of the MgTA@MnO_2 /GelMA platform (Figure 6E–J).

Osteoimmune Modulation of Bone Metabolism Homeostasis

To systematically evaluate the paracrine regulation of bone homeostasis by the reprogrammed immune microenvironment, an in vitro conditioned medium (CM) culture model was established (Figure 7A). Quantitative ELISA analysis of the CM derived from the MgTA@MnO_2/GelMA-treated macrophages revealed a profound suppression in the secretion of pro-inflammatory cytokines, specifically IL-17A, TNF-α, and IL-6 (Figure 7B–D). Concurrently, this inflammatory blockade was accompanied by a significant surge in the release of the reparative and anti-inflammatory cytokine IL-10 (Figure 7E).

When MC3T3-E1 pre-osteoblasts were cultured within this immunomodulatory CM, they exhibited accelerated osteogenic differentiation, evidenced by enhanced alkaline phosphatase (ALP) activity and extensive extracellular matrix mineralization (Figure 7F–I). Transcriptional profiling further corroborated these phenotypic changes, showing significant upregulation of core osteogenic driving genes, including Runx2, ALP, OSX, and BMP2 (Figure 7L). Conversely, the application of this same CM to RANKL-stimulated RAW264.7 cells exerted a potent anti-osteoclastogenic effect. It markedly suppressed the formation of TRAP-positive multinucleated mature osteoclasts and broadly downregulated the transcription of essential osteoclastogenic genes, such as NFATc1, CTSK, TRAP, and c-Fos (Figure 7J, K, M). Taken together, these results unequivocally demonstrate that the composite hydrogel actively dictates a favorable osteoimmune microenvironment, successfully coupling robust osteogenesis with inhibited osteoclastogenesis to restore skeletal homeostasis.

In vivo Trabecular Bone Regeneration in an Osteoporotic Defect Model

To rigorously evaluate the translational potential and localized osteogenic efficacy of the engineered hydrogel, an in vivo ovariectomized (OVX) rat model with distal femoral bone defects was established, closely mimicking a profound osteoporotic microenvironment (Figure 8A). The spatiotemporal progression of new bone formation within the structural voids was longitudinally monitored via high-resolution micro-computed tomography (micro-CT) at 4, 8, and 12 weeks post-implantation (Figure 8B). Quantitative 3D morphometric analyses demonstrated that the MgTA@MnO_2/GelMA hydrogel significantly accelerated trabecular bone regeneration over time. By week 12, the hydrogel-treated cohort exhibited markedly superior bone mineral density (BMD), an increased bone volume fraction (BV/TV), and elevated trabecular number (Tb.N), coupled with a substantial reduction in trabecular separation (Tb.Sp) compared to the untreated control and pristine GelMA groups (Figure 8C–F). These striking radiological findings were robustly corroborated by comprehensive histological evaluations. Hematoxylin and Eosin (H&E) and Masson's trichrome staining

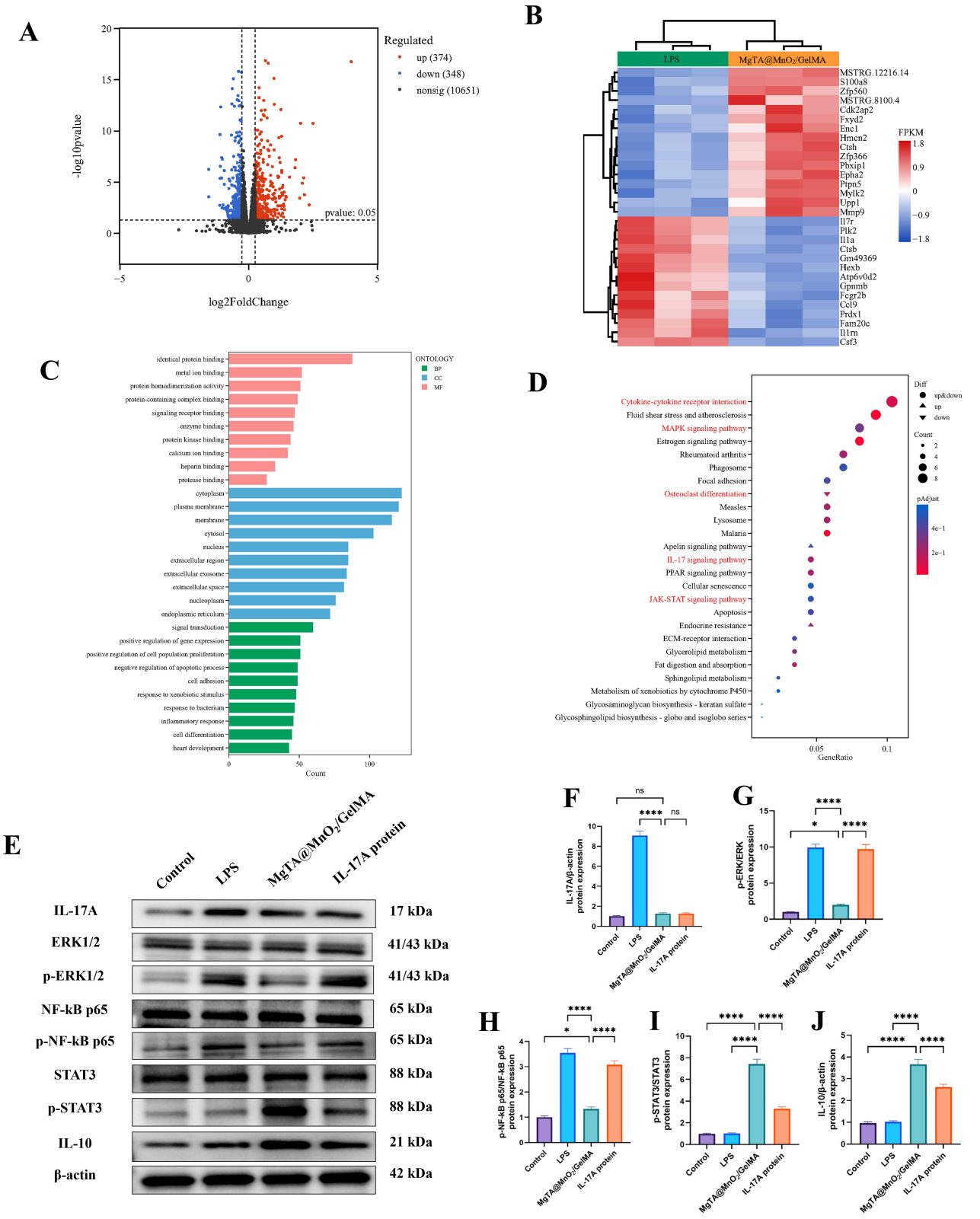

Figure 6 Transcriptomic profiling and mechanistic validation of the MgTA@MnO_2/GelMA-mediated macrophage immunomodulation. (**A**) Volcano plot and (**B**) hierarchical clustering heatmap illustrating the differentially expressed genes (DEGs) between the LPS-stimulated control and the MgTA@MnO_2/GelMA-treated RAW264.7 macrophages. Red and blue signify significantly upregulated and downregulated genes, respectively. (**C**) Gene Ontology (GO) functional enrichment analysis of the DEGs, categorized by biological processes, cellular components, and molecular functions. (**D**) Kyoto Encyclopedia of Genes and Genomes (KEGG) pathway enrichment bubble chart of the DEGs, highlighting the significant enrichment of critical immune-related cascades, specifically the IL-17 and MAPK signaling pathways. (**E–J**) Representative Western blot images (E) and corresponding densitometric quantification (F–J) of the core regulatory proteins within the identified signaling axes. Data are presented as mean ± SD (n = 3). *P < 0.05, ****P < 0.0001; ns indicates not significant.

https://doi.org/10.2147/IJN.S606744

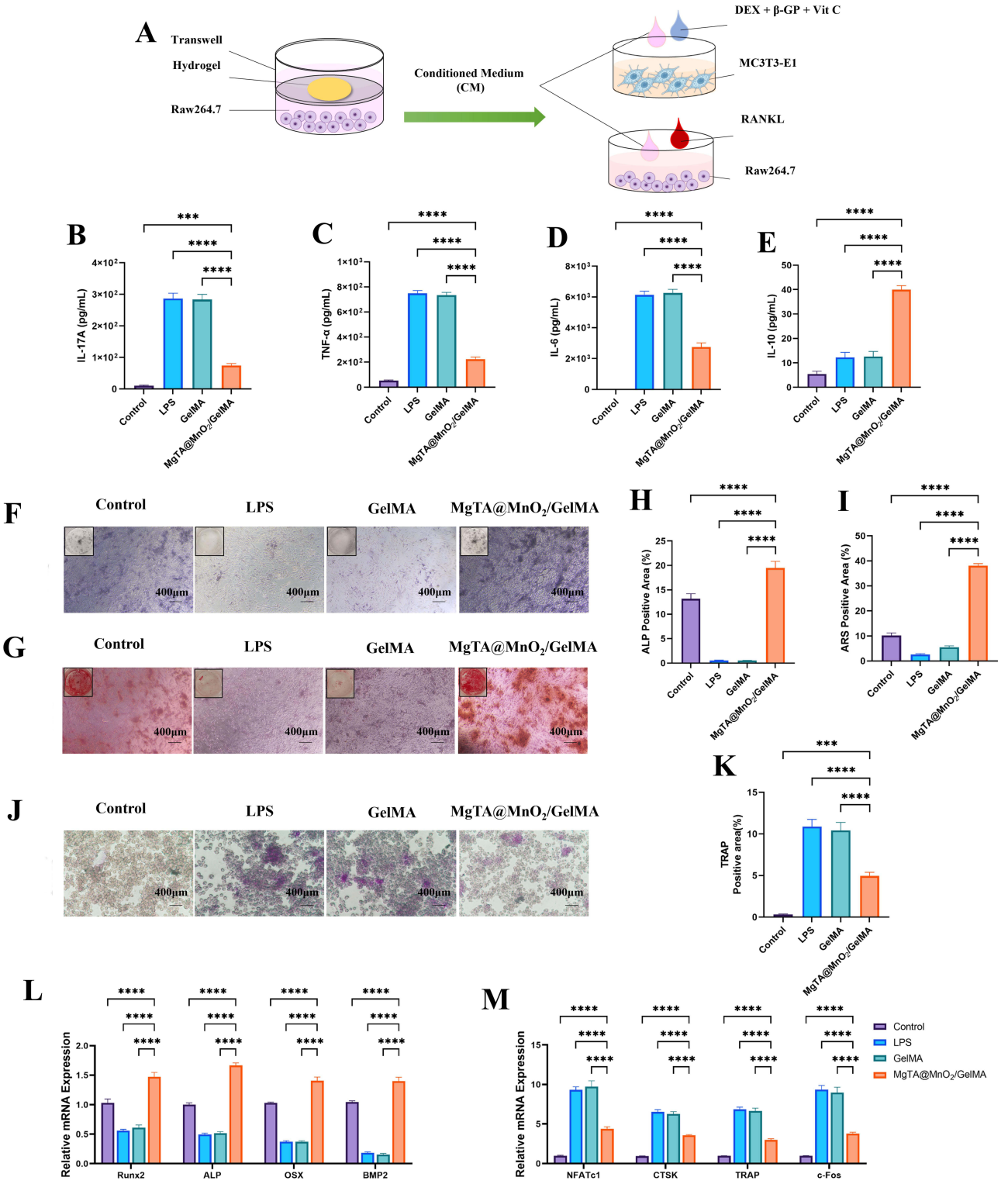

Figure 7 The MgTA@MnO_2/GelMA hydrogel orchestrates bone metabolism homeostasis via osteoimmunomodulation. (**A**) Schematic illustration of the experimental design utilizing conditioned media to evaluate the osteogenesis–osteoclastogenesis coupling. (**B–E**) Quantitative ELISA analysis of the pro-inflammatory and anti-inflammatory cytokine secretion profiles within the conditioned media. (**F** and **G**) Representative images of (F) alkaline phosphatase (ALP) and (G) Alizarin Red S (ARS) staining of MC3T3-E1 cells cultured under various conditioned media. The inset square boxes in the upper left corners of F and G display the macroscopic views of the entire stained wells. **(H** and **I**) Corresponding semi-quantitative evaluation of the ALP activity and ARS mineralization areas. (**J**) Representative images of tartrate-resistant acid phosphatase (TRAP) staining of RAW264.7 cells, assessing osteoclast differentiation. (**K**) Quantitative analysis of the TRAP-positive multinucleated osteoclasts. (**L** and **M)** Quantitative real-time PCR (qRT-PCR) gene expression analysis of (L) osteogenesis-related and (M) osteoclastogenesis-related markers. Data are presented as mean ± SD (n = 3). ***P < 0.001, ****P < 0.0001.

https://doi.org/10.2147/IJN.S606744

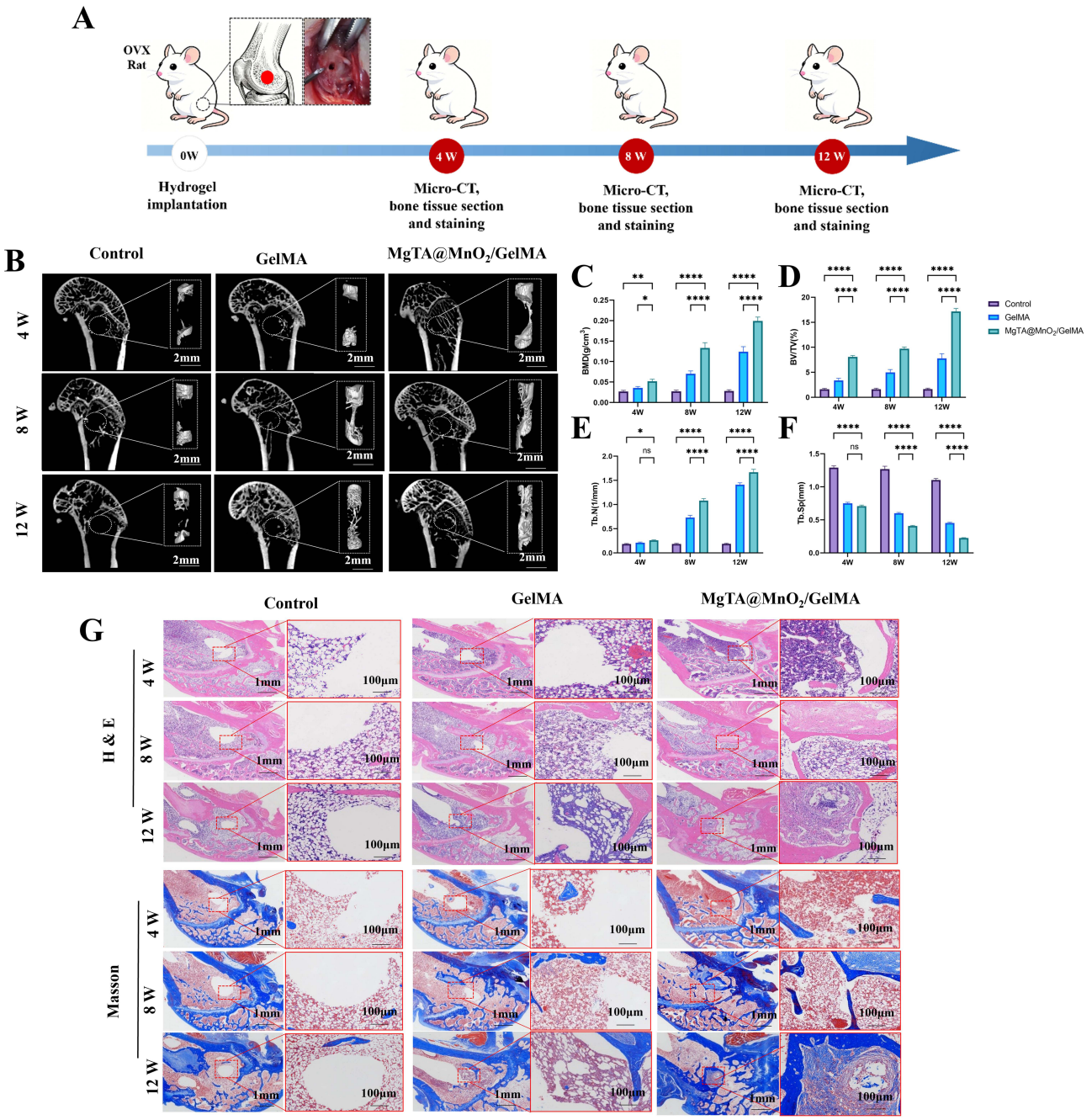

Figure 8 In vivo therapeutic efficacy of the MgTA@MnO_2/GelMA hydrogel for osteoporotic bone defect repair. **(A)** Schematic illustration of the surgical timeline and experimental protocol, encompassing the establishment of the ovariectomized (OVX) rat model, creation of the distal femoral defect, in situ hydrogel implantation, and subsequent tissue harvesting. (**B**) Representative three-dimensional (3D) micro-CT reconstructed images of the femoral defect regions across different treatment groups. The white dotted circles indicate the initial bone defect areas. (**C–F**) Quantitative micro-CT bone morphometric analyses of the newly formed trabecular bone microarchitecture. (**G**) Representative histological evaluations of the decalcified bone defect sections stained with Hematoxylin and Eosin (H&E) and Masson's trichrome (M&T), visualizing progressive new bone formation and collagen deposition. The red dashed square boxes indicate the regions of interest that are magnified in the adjacent right panels. Data are presented as mean ± SD (n = 6). *P < 0.05, **P < 0.01, ****P < 0.0001; ns indicates not significant.

revealed that the defect regions treated with the composite hydrogel were densely populated by highly organized, mature newly formed bone tissue and abundant, structurally aligned collagen deposition (Figure 8G). Collectively, these in vivo outcomes compellingly confirm that the immunomodulatory hydrogel provides a highly permissive microenvironment that successfully rescues osteoporotic bone loss and drives structural skeletal regeneration.

https://doi.org/10.2147/IJN.S606744

In vivo Mechanistic Validation of Osteoimmunomodulation and Systemic Biosafety

To elucidate the in vivo mechanisms driving the observed bone regeneration, the local osteoimmune and angiogenic microenvironments within the defect sites were mapped via immunofluorescence staining. Consistent with our in vitro findings, regions treated with the MgTA@MnO_2/GelMA hydrogel exhibited a striking reduction in the infiltration of pro-inflammatory $CD68^+$ M1 macrophages, concomitant with a robust accumulation of tissue-reparative $CD163^+$ M2 macrophages (Figure 9A–D). Driven by this successfully reprogrammed immunomodulatory niche, the localized expression of critical angiogenic and osteogenic markers, specifically VEGF and Osterix (OSX), was profoundly enhanced within the defect boundaries, demonstrating highly significant upregulation ($P < 0.0001$) compared to the control groups (Figure 9E–H). Finally, comprehensive histological examinations of major vital organs (heart, liver, spleen, lung, and kidneys) revealed no discernible pathological alterations, structural damage, or inflammatory lesions. These systemic evaluations robustly confirm the excellent physiological biosafety and high translational feasibility of the composite hydrogel platform for complex in vivo tissue engineering applications (Figure 9I).

Discussion

Achieving functional bone regeneration in osteoporotic patients is severely restricted by a complex pathological microenvironment. This local niche is defined by interconnected detrimental factors, primarily elevated oxidative stress, restricted vascular networks, and a chronically dysregulated immune response. Although recent biomaterial advancements address isolated aspects of these barriers, therapeutic strategies that concurrently resolve this multifactorial network remain clinically scarce. Our research framework prioritizes rational component integration over the pursuit of novel fundamental chemistries. By leveraging the inherent tunable and injectable properties of the methacrylated gelatin (GelMA) matrix, we constructed a composite hydrogel that strategically unites the established bioactivities of MnO_2 (catalase-mimetic catalysis), tannic acid (polyphenolic coordination), and magnesium ions (osteoimmunomodulation and angiogenesis) into a single delivery platform. The resulting data confirm that this composite system fundamentally remodels the local osteoimmune landscape. The targeted reprogramming of macrophage polarization serves as the primary biological driver for the observed enhancement in bone tissue repair.

Multifunctional Co-Design Strategy: A Rational Integrated Hydrogel System

Impaired healing in osteoporosis arises from a self-perpetuating pathological network involving disrupted redox homeostasis, insufficient vascularization, and a sustained inflammatory immune state.[26–28] Conventional biomaterials typically offer passive structural support but lack the distinct multifunctionality required to counteract these intertwined pathological drivers. Building upon recent strategies that incorporate solitary bioactive ions or drugs,[29–32] our study introduces a highly integrated material design paradigm. We synthesized a composite nanozyme (MgTA@MnO_2) via a streamlined in situ coordination process and subsequently embedded it as the active functional core within the GelMA network.

This architectural design synergistically merges the catalase-mimetic ROS scavenging activity of the MnO_2 core[33,34] with the intrinsic antioxidant and anti-inflammatory properties of TA. The TA component simultaneously acts as a stable chelating agent for Mg^{2+},[35,36] facilitating the controlled release of an ion known for its pro-osteogenic, pro-angiogenic,[23] and emerging immunomodulatory capabilities. [25,37] Comprehensive material characterization confirmed the successful coordination of these components (Figures 1 and 2). The resulting synergistic outcomes, notably the tailored mechanical properties (Figure 2E) and the sustained H_2O_2-decomposition capacity (Figure 2F), are direct consequences of the dynamic TA-Mg^{2+} metallophenolic network formed on the MnO_2 surface.[38–40] This defined materials-level synergy establishes the physical and chemical foundation necessary for eliciting complex, cascading biological responses.

The development of multifunctional nanozyme platforms represents a transformative frontier in regenerative medicine. Recent high-impact studies have demonstrated that integrating metal-organic frameworks or hierarchical cascade nanozymes can achieve remarkable efficacy in reactive oxygen species (ROS) scavenging and microenvironment remodeling.[41–43] However, while many existing platforms rely on relatively static catalytic mechanisms or exhibit undesirable burst-release profiles, our MgTA@MnO_2 system offers a distinct advantage through the implementation of a dynamic metal-phenolic network (MPN). This MPN architecture acts as a pH-responsive gatekeeper, facilitating the

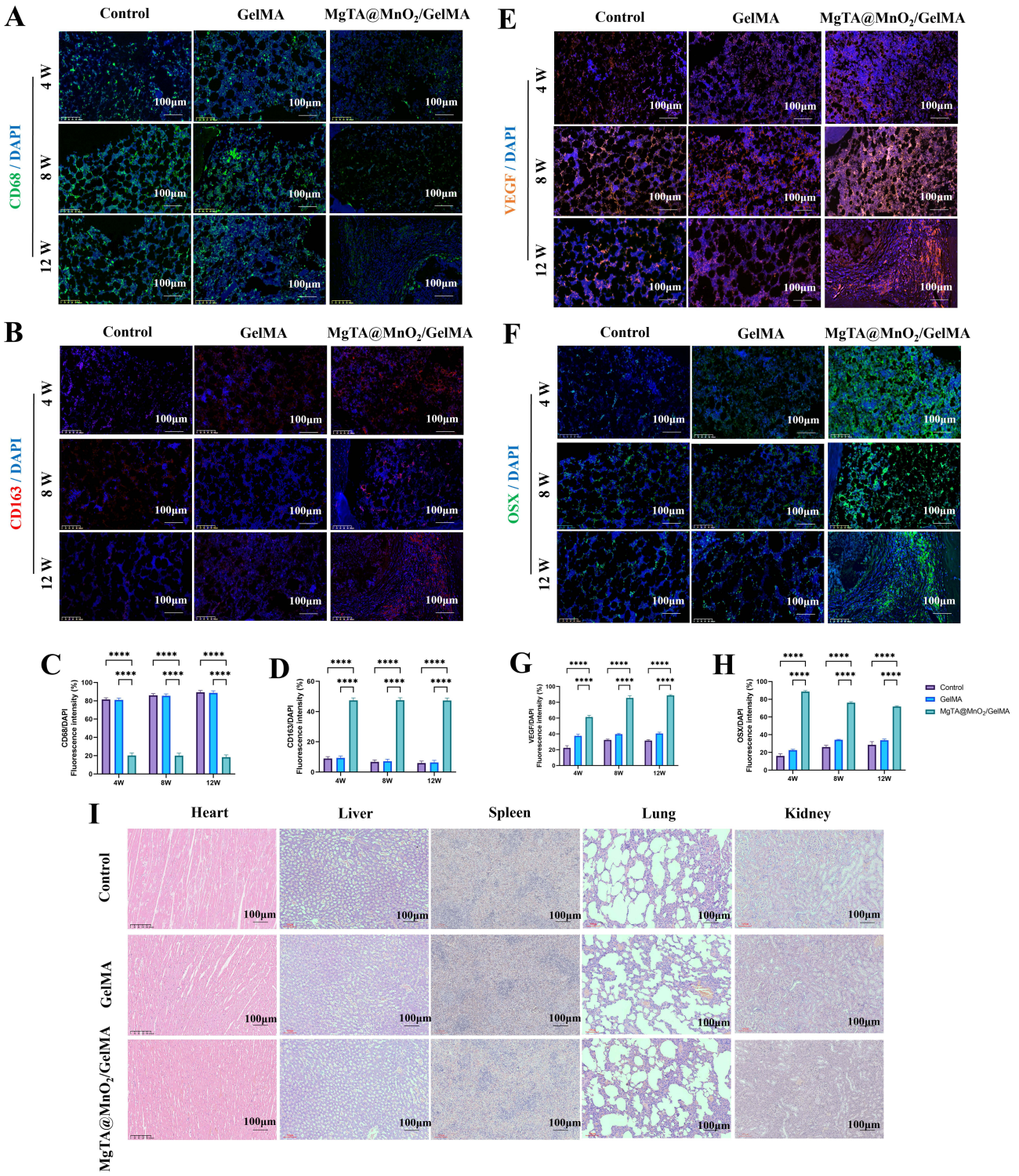

Figure 9 In vivo mechanistic validation of osteoimmunomodulation, angiogenesis, and systemic biosafety of the MgTA@MnO_2/GelMA hydrogel. (**A** and **B**) Representative immunofluorescence images detailing the macrophage phenotypic transition within the defect region (green: $CD68^+$ M1 macrophages; red: $CD163^+$ M2 macrophages), alongside (**C** and **D**) their corresponding semi-quantitative analyses. (**E** and **F**) Representative immunofluorescence staining and (**G** and **H**) subsequent semi-quantitative evaluation of the pro-angiogenic marker VEGF and the osteogenic marker Osterix (OSX) in the newly formed tissues. (**I**) Representative Hematoxylin and Eosin (H&E)-stained histological sections of major vital organs (heart, liver, spleen, lung, and kidneys) following the treatment period. The absence of discernible pathological alterations or inflammatory infiltration confirms the excellent systemic biosafety profile of the implanted biomaterials. Data are presented as mean ± SD (n = 6). ****P < 0.0001.

https://doi.org/10.2147/IJN.S606744

sustained and synchronized release of Mg^{2+} and TA. More importantly, it works in synergy with the catalase-mimetic MnO_2 core to enable bidirectional regulation of the IL-17/MAPK/NF-κB osteoimmune axis. This orchestrated multi-target intervention provides a more robust and comprehensive pharmacological strategy for accelerating bone repair under osteoporotic conditions.

Antioxidative Protection: Activating Endogenous Cell-Signaling Pathways

Oxidative stress disrupts bone healing in osteoporosis by inducing osteoblast apoptosis and severely impairing osteogenic differentiation.[44,45] The experimental results validate that the MgTA@MnO_2/GelMA hydrogel actively protects MC3T3-E1 pre-osteoblasts from H_2O_2-induced injury, strictly preserving mitochondrial membrane integrity (Figure 3D–I). Crucially, this cytoprotective mechanism extends well beyond simple extracellular ROS neutralization. Western blot analyses revealed a significant upregulation of the transcription factor NRF2 and its downstream protective effectors, HO-1 and NQO1, within the osteoblasts (Figure 3J–M). NRF2 operates as a master regulator of the cellular antioxidant defense system; its activation is fundamentally linked to the promotion of osteogenic gene expression and subsequent matrix mineralization.[46,47] This observation confirms that the nanozyme-hydrogel system functions as an intracellular signal transducer rather than merely an extracellular ROS sink. It effectively empowers the cells' intrinsic repair capacities by activating the endogenous NRF2 cascade. Furthermore, the localized release of Mg^{2+} likely provides a synergistic contribution to this process, as Mg^{2+} deficiency is clinically recognized to impair mitochondrial function and exacerbate intracellular oxidative damage.[48]

Pro-Angiogenic Effect: Fostering a Nutrient-Supply Network for Regeneration

Adequate and rapid vascularization is an absolute prerequisite for successful bone regeneration, ensuring the continuous delivery of oxygen, essential nutrients, and circulating regenerative cells to the defect site.[49,50] The data indicate that the MgTA@MnO_2/GelMA matrix markedly enhances the tube-forming and migratory capacities of HUVECs, corresponding with the explicit upregulation of core pro-angiogenic factors including VEGF, bFGF, and Angiopoietin-1 (Figure 4). This comprehensive vascular response is achieved through overlapping mechanisms. Direct ionic stimulation via Mg^{2+} inherently promotes endothelial cell proliferation and VEGF secretion.[51,52] Concurrently, by scavenging excessive ROS—a primary instigator of endothelial dysfunction—the hydrogel fosters a redox-balanced extracellular niche highly conducive to angiogenesis. Beyond these direct material effects, M2-polarized macrophages within the modulated microenvironment secrete additional pro-angiogenic paracrine factors.[53,54] This coordinated sequence, spanning precise material chemistry to targeted cellular modulation, constructs a localized microenvironment primed for neo-vessel formation.

Regulation of Macrophage Polarization: A Core Mechanism for Reshaping the Osteoimmune Microenvironment

A pivotal finding of this research is the pronounced regulatory control exerted by the MgTA@MnO_2/GelMA hydrogel over the osteoimmune microenvironment. The orchestrated phenotypic transition from pro-inflammatory M1 macrophages to tissue-reparative M2 macrophages is a recognized prerequisite for initiating proper tissue regeneration.[18,55] Under osteoporotic pathology, macrophages frequently arrest in the M1 state, continuously secreting inflammatory cytokines (eg, TNF-α, IL-1β, IL-6). This sustained inflammatory profile suppresses osteoblast activity while hyper-stimulating osteoclastogenesis, effectively stalling the repair cascade.[56–59]

Our evaluations confirm that the composite hydrogel significantly diminishes LPS-induced M1 polarization—evidenced by reduced iNOS and TNF-α expression—while concurrently driving a robust shift toward the M2 phenotype, marked by elevated CD206 and ARG-1 levels (Figure 5). Deeper mechanistic insights were extracted via transcriptomic profiling (Figure 6). KEGG enrichment and subsequent protein-level validations identified that the material specifically paralyzes the pro-inflammatory IL-17/MAPK/NF-κB axis.[60,61] IL-17A operates as a potent inflammatory mediator central to inflammatory bone loss.[7,62] The MgTA@MnO_2/GelMA treatment drastically downregulated IL-17A alongside its downstream effectors p-ERK and p-NF-κB p65. The observation that exogenous IL-17A supplementation partially

negated these therapeutic effects isolates the IL-17 signaling pathway as the primary target of the material's immunomodulatory action. Simultaneously, the hydrogel promoted the phosphorylation of STAT3 and the expression of IL-10, activating a critical signaling cascade required for stabilizing the M2 phenotype.[63,64] This targeted bidirectional regulation—suppressing inflammatory cascades while activating reparative pathways—ensures precise and comprehensive macrophage reprogramming.

Immunomodulation-Driven Bone-Metabolic Balance: From Cellular Phenotype to Functional Output

The transition of the macrophage phenotype dictates profound physiological consequences for local bone metabolism. Macrophages exposed to the composite material shift their paracrine secretory profiles from an inflammatory dominance (high IL-17A, TNF-α, IL-6) to a pro-reparative state characterized by elevated IL-10 (Figures 7B–E). Co-culture assays utilizing this optimized conditioned medium validated a core tenet of osteoimmunology: local immune cells function as the upstream regulators of bone metabolic balance.[65,66] The re-established immune microenvironment directly accelerated the osteogenic differentiation of MC3T3-E1 cells, significantly enhancing ALP activity, matrix mineralization, and osteogenic gene transcription. Conversely, this identical microenvironment actively suppressed the differentiation of RANKL-stimulated RAW264.7 cells into osteoclasts, reducing TRAP-positive multinucleated cell formation and downregulating critical osteoclastogenic genes (Figure 7F–M). These specific paracrine findings bridge materials science with osteoimmunology, offering an actionable strategy to correct the uncoupled bone formation and resorption characteristic of osteoporosis.

In vivo Bone-Repair Efficacy: Integrated Manifestation of Multi-Mechanism Synergy

Implantation of the MgTA@MnO_2/GelMA hydrogel into femoral defects of an established OVX rat model translated these in vitro mechanisms into significant in vivo bone regeneration (Figure 8). Quantitative micro-CT measurements (BMD, BV/TV, Tb.N, Tb.Sp) combined with histological mapping of new bone tissue and organized collagen deposition objectively established the material's superior osteogenic performance. In vivo mechanistic mapping (Figure 9) precisely mirrored the isolated in vitro pathways. The treated defect regions exhibited a dense infiltration of reparative M2 macrophages ($CD163^+$), robust neovascularization networks ($VEGF^+$), and elevated local osteogenic activity (OSX^+), matched by a sharp decline in inflammatory M1 macrophage presence ($CD68^+$). This in vivo evidence illustrates a seamless reparative continuum: targeted ROS scavenging triggers macrophage polarization, which reshapes the immune microenvironment, subsequently fostering vascularization and driving synergistic osteogenesis.

Study Limitations and Future Perspectives

While this study establishes a robust immunomodulatory framework, several limitations require future clarification. The current investigation focuses exclusively on macrophage populations; however, the broader osteoimmune network encompasses T cells, B cells, and neutrophils, all of which participate in bone metabolic regulation.[7,20] The explicit influence of the composite material on these distinct immune subsets warrants comprehensive mapping. Additionally, while optimal repair outcomes and systemic biosafety were recorded over the 12-week observational window, extended temporal evaluations are necessary. Long-term studies must assess the material's ultimate degradation profile, the physiological clearance of the released Mn and Mg ions, and the precise histological quality of the regenerated trabecular and cortical structures. Methodologically, plasma quenching phenomena in ICP-OES/MS restricted the precise quantification of individual release kinetics for TA, Mg^{2+}, and MnO_2 from the GelMA matrix. Furthermore, while our integrated MgTA@MnO_2 system demonstrated robust therapeutic efficacy, the current study lacks isolated single-component controls (eg, Mg/GelMA and TA/GelMA) in the biological assays. Although previous studies have independently and extensively confirmed the partial osteogenic and pro-angiogenic benefits of solitary Mg^{2+} treatments,[67,68] as well as the potent antioxidant and immunomodulatory properties of TA-based hydrogels,[69,70] highly controlled omission experiments are necessary in future studies. Such evaluations will precisely delineate the individual biological contribution of each constituent versus their synergistic effects within the full platform. Finally, advancing this platform toward

clinical translation mandates rigorous efficacy and load-bearing evaluations within large-animal osteoporotic defect models.

Future developmental trajectories will focus on employing single-cell RNA sequencing to comprehensively map the dynamic transcriptional profiles of the entire immune and stromal cell population within the defect site. Furthermore, engineering the hydrogel matrix to exhibit microenvironment-responsive degradation (eg, precise ROS- or pH-triggered release) could achieve superior spatiotemporal control over ion and polyphenol delivery, maximizing the therapeutic window for osteoporotic bone repair.

Conclusion

In conclusion, we have rationally designed and constructed a multifunctional MgTA@MnO_2/GelMA composite hydrogel as a highly potent osteoimmunomodulatory platform for the treatment of osteoporotic bone defects. Mechanistically, the integrated MgTA@MnO_2 nanozymes actively reprogram the hostile immune microenvironment by driving macrophage polarization toward a pro-reparative M2 phenotype. Supported by transcriptomic profiling, we identified that this immunomodulation is achieved via the targeted blockade of the IL-17A/MAPK/NF-κB inflammatory axis. Consequently, this restored immune homeostasis paracrinally orchestrates a highly permissive regenerative niche, successfully coupling enhanced angiogenesis and robust osteogenesis with profoundly suppressed osteoclastogenesis. In vivo evaluations in an ovariectomized (OVX) rat model demonstrated accelerated, high-quality trabecular bone regeneration alongside excellent systemic biosafety. Ultimately, this paradigm-shifting "osteoimmune-rebalancing" strategy not only provides a highly translational biomaterial solution for osteoporotic fractures but also offers profound insights into the design of next-generation immunotherapeutics for complex inflammatory skeletal diseases.

Data Sharing Statement

The datasets used and/or analyzed during the current study are available from the corresponding author upon reasonable request.

Ethics Approval and Consent to Participate

The animal protocols were approved by the Experimental Animal Welfare and Ethics Committee of Wannan Medical University, Wuhu city (No. WNMC-AWE-2025323). All animal procedures, including housing, anesthesia, and euthanasia, were performed in strict accordance with the National Institutes of Health Guide for the Care and Use of Laboratory Animals and fully complied with the American Veterinary Medical Association (AVMA) Guidelines for the Euthanasia of Animals.

Clinical trial number: not applicable.

Acknowledgments

We would like to express our gratitude to the Central Laboratory of Yijishan Hospital and the Anhui Provincial Key Laboratory for Non-coding RNA Translational Research on Major Diseases for providing the necessary instruments and facilities for this study.

Author Contributions

Yifan Gu and Lei Li contributed equally to this work. All authors made a significant contribution to the work reported, whether that is in the conception, study design, execution, acquisition of data, analysis and interpretation, or in all these areas; took part in drafting, revising or critically reviewing the article; gave final approval of the version to be published; have agreed on the journal to which the article has been submitted; and agree to be accountable for all aspects of the work.

Funding

This research was supported by Talent Introduction Project of Yijishan Hospital, Wannan Medical University (Grant No. KY29240723), Anhui Province Higher Education Science Research Project (Grant No. 2025AHGXZK31385), Anhui Province Higher Education Science Research Project (Grant No. 2023AH040265), Anhui Clinical Medical Research

Transformation Project (Grant No. 202304295107020007), Talented Scholars of Wannan Medical University (Grant No. YR202226), Technology Mountaineering Program of Yijishan Hospital, Wannan Medical University (Grant No. PF2019005), and Research project of Anhui Provincial Health Commission (Grant No. AHWJ2023A10149).

Disclosure

The authors declare that they have no known competing financial interests or personal relationships that could have appeared to influence the work reported in this paper.

References

1. Compston JE, McClung MR, Leslie WD. Osteoporosis. *Lancet*. 2019;393(10169):364–376. doi:10.1016/S0140-6736(18)32112-3
2. Hong N, Whittier DE, Glüer CC, Leslie WD. The potential role for artificial intelligence in fracture risk prediction. *Lancet Diabetes Endocrinol*. 2024;12(8):596–600. doi:10.1016/S2213-8587(24)00153-0
3. Li W, Jiang WS, Su YR, et al. PINK1/Parkin-mediated mitophagy inhibits osteoblast apoptosis induced by advanced oxidation protein products. *Cell Death Dis*. 2023;14(2):88. doi:10.1038/s41419-023-05595-5
4. Iantomasi T, Romagnoli C, Palmini G, et al. Oxidative stress and inflammation in osteoporosis: molecular mechanisms involved and the relationship with microRNAs. *IJMS*. 2023;24(4):3772. doi:10.3390/ijms24043772
5. Puthiyoth Dayanandan A, Prakash N, Arai Y, Kim BJ, Lee SH. Biomaterials-based engineering of the bone microenvironment for osteoporosis therapy. *J Tissue Eng*. 2026;17:20417314251413982. doi:10.1177/20417314251413982
6. Yao Y, Cai X, Chen Y, Zhang M, Zheng C. Estrogen deficiency-mediated osteoimmunity in postmenopausal osteoporosis. *Med Res Rev*. 2025;45(2):561–575. doi:10.1002/med.22081
7. Fischer V, Haffner-Luntzer M. Interaction between bone and immune cells: implications for postmenopausal osteoporosis. *Semin Cell Dev Biol*. 2022;123:14–21. doi:10.1016/j.semcdb.2021.05.014
8. Lu W, Zeng M, Liu W, et al. Human urine-derived stem cell exosomes delivered via injectable GelMA templated hydrogel accelerate bone regeneration. *Mater Today Bio*. 2023;19:100569. doi:10.1016/j.mtbio.2023.100569
9. Zhou B, Jiang X, Zhou X, et al. GelMA-based bioactive hydrogel scaffolds with multiple bone defect repair functions: therapeutic strategies and recent advances. *Biomater Res*. 2023;27(1):86. doi:10.1186/s40824-023-00422-6
10. Yu H, Luo X, Li Y, et al. Advanced hybrid strategies of GelMA composite hydrogels in bone defect repair. *Polymers*. 2024;16(21):3039. doi:10.3390/polym16213039
11. Mou X, Wu Q, Zhang Z, et al. Nanozymes for regenerative medicine. *Small Methods*. 2022;6(11):2200997. doi:10.1002/smtd.202200997
12. Wu Y, Zhou Z, Zhang M, Li S, Sun M, Song Z. Hollow manganese dioxide-chitosan hydrogel for the treatment of atopic dermatitis through inflammation-suppression and ROS scavenging. *J Nanobiotechnol*. 2023;21(1):432. doi:10.1186/s12951-023-02174-w
13. Fu X, Luo Z, Guo Y, et al. Microenvironment-responsive multifunctional enzyme-linked hydrogel for diabetic bone defect regeneration. *Nat Commun*. 2025;16(1):10275. doi:10.1038/s41467-025-65165-5
14. Sun D, Ding C, Wang N, et al. Near-infrared responsive nanozyme-carboxymethyl chitosan/chondroitin sulfate composite hydrogel: multi-component synergy optimizes bone defect microenvironment to enhance repair. *Int J Biol Macromol*. 2025;332:148646. doi:10.1016/j.ijbiomac.2025.148646
15. Xiao Y, Xu M, Shi Y, et al. ZnCe-LDO nanozyme-based multifunctional hydrogel promotes bone regeneration by inflammatory macrophage reprogramming and piezo1 activation. *ACS Nano*. 2025;19(36):32606–32628. doi:10.1021/acsnano.5c10123
16. Wang Z, Gu C, Tang Y, et al. Bioactive multifunctional hydrogel scaffolds remodel the inflammatory microenvironment and osteogenic-osteoclastic homeostasis to advance osteoporotic bone defect repair. *ACS Nano*. 2025;19(50):42538–42555. doi:10.1021/acsnano.5c15635
17. Yang N, Liu Y. The role of the immune microenvironment in bone regeneration. *Int J Med Sci*. 2021;18(16):3697–3707. doi:10.7150/ijms.61080
18. Schlundt C, Fischer H, Bucher CH, Rendenbach C, Duda GN, Schmidt-Bleek K. The multifaceted roles of macrophages in bone regeneration: a story of polarization, activation and time. *Acta Biomater*. 2021;133:46–57. doi:10.1016/j.actbio.2021.04.052
19. Cai G, Ren L, Yu J, et al. A microenvironment-responsive, controlled release hydrogel delivering embelin to promote bone repair of periodontitis via anti-infection and osteo-immune modulation. *Adv Sci*. 2024;11(34):2403786. doi:10.1002/advs.202403786
20. Qi Z, Luo J, Xiao Z, Yang D. Functional roles of immune cells in osteoporosis. *Front Immunol*. 2025;16:1698283. doi:10.3389/fimmu.2025.1698283
21. Zhou G, Zhou Q, Li R, et al. Synthetically engineered bacterial extracellular vesicles and IL-4-encapsulated hydrogels sequentially promote osteoporotic fracture repair. *ACS Nano*. 2025;19(16):16064–16083. doi:10.1021/acsnano.5c03106
22. Cai Z, Bai L, Li Q, Li Y, Cai X, Lin Y. Gene-activating framework nucleic acid-targeted upregulating sirtuin-1 to modulate osteoimmune microenvironment for diabetic osteoporosis therapeutics. *ACS Nano*. 2024;18(52):35214–35229. doi:10.1021/acsnano.4c08727
23. Gu Y, Zhang J, Zhang X, Liang G, Xu T, Niu W. Three-dimensional printed Mg-doped β-TCP bone tissue engineering scaffolds: effects of magnesium ion concentration on osteogenesis and angiogenesis in vitro. *Tissue Eng Regen Med*. 2019;16(4):415–429. doi:10.1007/s13770-019-00192-0
24. Lin KY, Wu YF, Aung LM, et al. Magnesium-enhanced porcine particles using hydrothermal technique improve the osteogenic differentiation of cells. *RSC Adv*. 2024;14(40):29455–29463. doi:10.1039/D4RA03496A
25. Li J, Ke H, Lei X, et al. Controlled-release hydrogel loaded with magnesium-based nanoflowers synergize immunomodulation and cartilage regeneration in tendon-bone healing. *Bioact Mater*. 2024;36:62–82. doi:10.1016/j.bioactmat.2024.02.024
26. Gu C, Zhou Q, Hu X, et al. Melatonin rescues the mitochondrial function of bone marrow-derived mesenchymal stem cells and improves the repair of osteoporotic bone defect in ovariectomized rats. *J Pineal Res*. 2024;76(1):e12924. doi:10.1111/jpi.12924
27. Li J, Du Y, Wang J, et al. Optimizing type H vessels formation via short fibers 3D scaffolds with maintaining redox homeostasis for osteoporotic bone remodeling. *Bioact Mater*. 2025;53:417–432. doi:10.1016/j.bioactmat.2025.07.030

28. Yang X, Wang Q, Yan C, et al. A dual-functional strontium-decorated titanium implants that guides the immune response for osseointegration of osteoporotic rats. *Colloids Surf B*. 2024;233:113643. doi:10.1016/j.colsurfb.2023.113643
29. Huang L, Guo Z, Yang X, et al. Advancements in GelMA bioactive hydrogels: strategies for infection control and bone tissue regeneration. *Theranostics*. 2025;15(2):460–493. doi:10.7150/thno.103725
30. Lei M, Liu H, Zhong Q, et al. Hydroxybutyl chitosan-based thermosensitive hydrogel enhanced osteoporotic bone regeneration through sustained release of alendronate and BMP-2. *Carbohydr Polym*. 2026;373:124609. doi:10.1016/j.carbpol.2025.124609
31. He Y, Zeng F, Quan H, et al. Strontium-loaded multifunctional gelatin methacryloyl hydrogels for type-H vascularized bone regeneration under osteoporotic conditions. *Mater Today Bio*. 2025;32:101909. doi:10.1016/j.mtbio.2025.101909
32. Ma Y, Su H, Li W, et al. The hyaluronic acid-gelatin hierarchical hydrogel for osteoporotic bone defect repairment. *Int J Biol Macromol*. 2024;276:133821. doi:10.1016/j.ijbiomac.2024.133821
33. Song Q, Wang D, Li H, et al. Dual-response of multi-functional microsphere system to ultrasound and microenvironment for enhanced bone defect treatment. *Bioact Mater*. 2024;32:304–318. doi:10.1016/j.bioactmat.2023.10.007
34. Yang Y, Yao Z, Sun Y, et al. 3D-printed manganese dioxide incorporated scaffold promotes osteogenic-angiogenic coupling for refractory bone defect by remodeling osteo-regenerative microenvironment. *Bioact Mater*. 2025;44:354–370. doi:10.1016/j.bioactmat.2024.10.019
35. Qi F, Xu Y, Zheng B, et al. The core-shell microneedle with probiotic extracellular vesicles for infected wound healing and microbial homeostasis restoration. *Small*. 2024;20(46):2401551. doi:10.1002/smll.202401551
36. Kuang Z, Cai X, Li B, et al. Fabrication and properties of multi-functional of tannic acid-modified sodium alginate/chitosan microspheres for bone defect repair. *Ann Biomed Eng*. 2025;53(9):2080–2094. doi:10.1007/s10439-025-03796-x
37. Zhou H, He Z, Cao Y, et al. An injectable magnesium-loaded hydrogel releases hydrogen to promote osteoporotic bone repair via ROS scavenging and immunomodulation. *Theranostics*. 2024;14(9):3739–3759. doi:10.7150/thno.97412
38. Wang Y, Chen Y, Zhou T, et al. A novel multifunctional nanocomposite hydrogel orchestrates the macrophage reprogramming-osteogenesis crosstalk to boost bone defect repair. *J Nanobiotechnol*. 2024;22(1):702. doi:10.1186/s12951-024-02996-2
39. Xin L, Li X, Yang Y, et al. Polyphenol and metal ion-reinforced supermolecular hydrogels incorporating nanofiber drug and peptide for annulus fibrosus regeneration. *Theranostics*. 2025;15(12):5756–5771. doi:10.7150/thno.106913
40. Xu B, Huang M, Li J, et al. The MnO2/GelMA composite hydrogels improve the ROS microenvironment of annulus fibrosus cells by promoting the antioxidant and autophagy through the SIRT1/NRF2 pathway. *Gels*. 2024;10(5):333. doi:10.3390/gels10050333
41. Meng Z, Zeng Z, Zhang Z, et al. Osteogenic nanozymes for diabetic bone regeneration via synergistic antioxidant and osteoinductive functions. *Adv Mater*. 2026;22:e72833. doi:10.1002/adma.72833
42. Huang Z, Jiang X, Zhang L, et al. Multifunctional manganese-based nanogels catalyze immune energy metabolism to promote bone repair. *Composites Part B*. 2025;291:112005. doi:10.1016/j.compositesb.2024.112005
43. Li Y, Muhammad F, Chen X, et al. Smart multifunctional Cu2O@RuO2 nanozyme for angiogenesis and osteogenesis in periodontitis. *Nano Today*. 2025;61:102624. doi:10.1016/j.nantod.2024.102624
44. Huang L, Zhang S, Bian M, et al. Injectable, anti-collapse, adhesive, plastic and bioactive bone graft substitute promotes bone regeneration by moderating oxidative stress in osteoporotic bone defect. *Acta Biomater*. 2024;180:82–103. doi:10.1016/j.actbio.2024.04.016
45. Zhou Q, Chen W, Gu C, et al. Selenium-modified bone cement promotes osteoporotic bone defect repair in ovariectomized rats by restoring GPx1-mediated mitochondrial antioxidant functions. *Regener Biomater*. 2023;10:rbad011. doi:10.1093/rb/rbad011
46. Onoki T, Kanczler J, Rawlings A, et al. Modulation of osteoblastogenesis by NRF2: NRF2 activation suppresses osteogenic differentiation and enhances mineralization in human bone marrow-derived mesenchymal stromal cells. *FASEB J*. 2024;38(17):e23892. doi:10.1096/fj.202400602R
47. Xi X, Li Z, Liu H, Chen S, Liu D. Nrf2 activation is involved in cyclic mechanical stress-stimulated osteogenic differentiation in periodontal ligament stem cells via PI3K/Akt signaling and HO1-SOD2 interaction. *Front Cell Dev Biol*. 2022;9:816000. doi:10.3389/fcell.2021.816000
48. Liu L, Wang F, Song W, et al. Magnesium promotes vascularization and osseointegration in diabetic states. *Int J Oral Sci*. 2024;16(1):10. doi:10.1038/s41368-023-00271-y
49. Tuckermann J, Adams RH. The endothelium–bone axis in development, homeostasis and bone and joint disease. *Nat Rev Rheumatol*. 2021;17(10):608–620. doi:10.1038/s41584-021-00682-3
50. Qin Q, Lee S, Patel N, et al. Neurovascular coupling in bone regeneration. *Exp Mol Med*. 2022;54(11):1844–1849. doi:10.1038/s12276-022-00899-6
51. Kang Y, Xu C, Meng L, Dong X, Qi M, Jiang D. Exosome-functionalized magnesium-organic framework-based scaffolds with osteogenic, angiogenic and anti-inflammatory properties for accelerated bone regeneration. *Bioact Mater*. 2022;18:26–41. doi:10.1016/j.bioactmat.2022.02.012
52. Gong Y, Wang P, Cao R, et al. Exudate absorbing and antimicrobial hydrogel integrated with multifunctional curcumin-loaded magnesium polyphenol network for facilitating burn wound healing. *ACS Nano*. 2023;17(22):22355–22370. doi:10.1021/acsnano.3c04556
53. Xiong Y, Lin Z, Bu P, et al. A whole-course-repair system based on neurogenesis-angiogenesis crosstalk and macrophage reprogramming promotes diabetic wound healing. *Adv Mater*. 2023;35(19):2212300. doi:10.1002/adma.202212300
54. Martin P, Gurevich DB. Macrophage regulation of angiogenesis in health and disease. *Semin Cell Dev Biol*. 2021;119:101–110. doi:10.1016/j.semcdb.2021.06.010
55. Chen L, Yu C, Xiong Y, et al. Multifunctional hydrogel enhances bone regeneration through sustained release of stromal cell-derived factor-1α and exosomes. *Bioact Mater*. 2023;25:460–471. doi:10.1016/j.bioactmat.2022.07.030
56. Cai W, Zhang J, Yu Y, et al. Mitochondrial transfer regulates cell fate through metabolic remodeling in osteoporosis. *Adv Sci*. 2023;10(4):2204871. doi:10.1002/advs.202204871
57. Luo J, Li L, Shi W, Xu K, Shen Y, Dai B. Oxidative stress and inflammation: roles in osteoporosis. *Front Immunol*. 2025;16:1611932. doi:10.3389/fimmu.2025.1611932
58. Tao H, Li W, Zhang W, et al. Urolithin A suppresses RANKL-induced osteoclastogenesis and postmenopausal osteoporosis by, suppresses inflammation and downstream NF-κB activated pyroptosis pathways. *Pharmacol Res*. 2021;174:105967. doi:10.1016/j.phrs.2021.105967
59. Cheng CH, Chen LR, Chen KH. Osteoporosis due to hormone imbalance: an overview of the effects of estrogen deficiency and glucocorticoid overuse on bone turnover. *IJMS*. 2022;23(3):1376. doi:10.3390/ijms23031376
60. Zhou H, He J, Liu R, et al. Microenvironment-responsive metal-phenolic network release platform with ROS scavenging, anti-pyroptosis, and ECM regeneration for intervertebral disc degeneration. *Bioact Mater*. 2024;37:51–71. doi:10.1016/j.bioactmat.2024.02.036

61. Zhao J, Peng G, Xiao D, et al. Yishen Qianggu Mixture formulation suppresses osteometabolic inflammation by modulating the IL-17/NF-κB/MAPK signaling axis. *J Ethnopharmacol*. 2026;358:121011. doi:10.1016/j.jep.2025.121011
62. Peng R, Dong Y, Zheng M, et al. IL-17 promotes osteoclast-induced bone loss by regulating glutamine-dependent energy metabolism. *Cell Death Dis*. 2024;15(2):111. doi:10.1038/s41419-024-06475-2
63. Sun Z, Xu Y, Shao B, et al. Exosomal circPOLQ promotes macrophage M2 polarization via activating IL-10/STAT3 axis in a colorectal cancer model. *J Immunother Cancer*. 2024;12(5):e008491. doi:10.1136/jitc-2023-008491
64. Zeng H, Zhao B, Zhang D, et al. Viola yedoensis Makino formula alleviates DNCB-induced atopic dermatitis by activating JAK2/STAT3 signaling pathway and promoting M2 macrophages polarization. *Phytomedicine*. 2022;103:154228. doi:10.1016/j.phymed.2022.154228
65. Yao Y, Cai X, Ren F, et al. The macrophage-osteoclast axis in osteoimmunity and osteo-related diseases. *Front Immunol*. 2021;12:664871. doi:10.3389/fimmu.2021.664871
66. Yang J, Gong X, Li T, et al. Tantalum particles promote M2 macrophage polarization and regulate local bone metabolism via macrophage-derived exosomes influencing the fates of BMSCs. *Adv Healthcare Mater*. 2024;13(17):2303814. doi:10.1002/adhm.202303814
67. Chen Z, Yang D, Wang S, Hao C. The role of magnesium hydrogels in bone regeneration: a systematic review and meta-analysis. *J Mater Sci*. 2025;36(1):66. doi:10.1007/s10856-025-06881-8
68. Zhou H, Yu K, Jiang H, et al. A three-in-one strategy: injectable biomimetic porous hydrogels for accelerating bone regeneration via shape-adaptable scaffolds, controllable magnesium ion release, and enhanced osteogenic differentiation. *Biomacromolecules*. 2021;22(11):4552–4568. doi:10.1021/acs.biomac.1c00842
69. Luo Y, Lin J, Luo X, et al. Tannic acid-programmed hydroxyapatite biomineralization enables bilayered bone-mimetic hydrogels for mandibular regeneration. *Chem Mater*. 2025;37(10):3853–3869. doi:10.1021/acs.chemmater.5c00840
70. Wang R, He X, Su S, Bai J, Liu H, Zhou F. Multifunctional tannic acid-based nanocomposite methacrylated silk fibroin hydrogel with the ability to scavenge reactive oxygen species and reduce inflammation for bone regeneration. *Int J Biol Macromol*. 2024;266:131357. doi:10.1016/j.ijbiomac.2024.131357